

---

Comparison of methods for  
quantitative analysis of dynamic  
susceptibility contrast enhanced  
brain perfusion MRI

*M.Sc. Thesis*

Bianca Maan

---

University of Twente  
Department of Electrical Engineering,  
Mathematics & Computer Science (EEMCS)  
Signals & Systems Group (SAS )  
P.O. Box 217  
7500 AE Enschede  
The Netherlands

BME Report Number: BME 032  
SAS Report Number: SAS 2010-10  
Report Date: 08/11/10  
Period of Work: 14/12/2009 – 08/11/10  
Thesis Committee: Prof. Dr. ir. C.H. Slump  
A.R. Lopes Simões, M.Sc.  
Dr. A. van Cappellen van Walsum



University of Twente  
Department of Electrical Engineering, Mathematics & Computer Science  
(EEMCS)  
Signals & Systems Group (SAS)

**Comparison of methods for quantitative analysis  
of dynamic susceptibility contrast enhanced brain  
perfusion MRI**

Vergelijking van methodes voor kwantitatieve analyse van dynamic  
susceptibility contrast brein perfusie MRI

*(met een samenvatting in het Nederlands)*

Master of Science Thesis  
BME 032 - SAS 2010-10

Bianca Maan  
November 8, 2010

**Thesis committee:**

Prof. Dr. ir. C.H. Slump  
A.R. Lopes Simões, M.Sc.  
Dr. A. van Cappellen van Walsum



“The beginning is the most important part of the work.”

*Plato*



---

# Abstract

Quantitative cerebral blood flow (CBF) can be obtained from dynamic susceptibility contrast (DSC) MRI using for instance the truncated singular value decomposition (tSVD). Block-circulant SVD and reformulated SVD (rSVD) are modified SVD approaches. The purpose of this study is to compare the different approaches. The optimal truncation thresholds ( $P_{SVD}$ ) for tSVD and block-circulant SVD are determined using simulated data. The optimal  $P_{SVD}$  minimizes the CBF estimation error over all residue functions and CBF values. The observed optimal  $P_{SVD}$  values are comparable to the values published by other authors.

Most authors assume that the recirculation in the concentration curves has to be removed. Using noise-free curves the CBF estimates are independent of the recirculation. However, when noise is added, a shift in optimal  $P_{SVD}$  occurs. Selecting the  $P_{SVD}$  of curves without recirculation will cause underestimation of the curves with recirculation.

The methods are compared in their ability to reproduce CBF. The determination of the  $P_{SVD}$  per voxel using generalized cross validation and L-curve criterion is investigated as well. The tSVD approach with the optimal fixed  $P_{SVD}$  performs best. In the presence of negative delays, the tSVD approach overestimates the CBF. Block-circulant and rSVD are delay-independent. Due to its delay dependent behavior, the tSVD approach performs worse in the presence of dispersion as well. However all SVD approaches are dependent on the amount of dispersion.

Furthermore different CBV calculation methods are compared: integration of the whole time signal, integration of the first pass, fitting of a gamma variate function and integration of the area under the tissue impulse response function obtained during deconvolution. The latter method performs best for all CBF, CBV and SNR values.

Using clinical data, large variations in the CBF values obtained with the methods and between tissue regions are observed.

After the comparisons it can be concluded that block-circulant SVD is the most promising approach due to the delay independent behavior.



---

# Samenvatting

Met truncated singular value decomposition (tSVD) kunnen kwantitatieve cerebral blood flow (CBF) waarden berekend worden uit dynamic susceptibility contrast (DSC) MRI data. Block-circulant SVD en reformulated SVD (rSVD) zijn aangepaste SVD methodes. Het doel van deze studie is het vergelijken van de methodes. De optimale thresholds ( $P_{SVD}$ ) voor tSVD en block-circulant SVD zijn bepaald met gesimuleerde data. De optimale  $P_{SVD}$  minimaliseert the CBF error voor alle residue functies en CBF waardes. De gevonden  $P_{SVD}$  waarden komen overeen met de literatuur.

De meeste onderzoekers nemen aan dat bloed recirculatie uit de curves verwijderd moet worden. Met ruis vrije curves zijn de CBF schattingen onafhankelijk van de recirculatie. Wanneer ruis toegevoegd wordt is er een verschuiving in optimale  $P_{SVD}$  zichtbaar. De  $P_{SVD}$  van curves zonder recirculatie zorgt voor onderschatting van de curves met recirculatie.

Vervolgens is de accuraatheid van de methodes vergeleken. Verder is de  $P_{SVD}$  per voxel met behulp van generalized cross validation en L-curve criterion onderzocht. De tSVD methode gecombineerd met de optimale vaste  $P_{SVD}$  geeft de beste CBF waarden. Bij negatieve vertragingen overschat de tSVD methode de CBF. De block-circulant en rSVD methode zijn onafhankelijk van de vertraging. Door het vertraging afhankelijke gedrag van tSVD presteert deze methode ook het slechtste bij aanwezigheid van dispersie. Echter alle SVD methodes zijn afhankelijk van de hoeveelheid dispersie.

Verder zijn er verschillende CBV bereken methodes vergeleken: integratie over de gehele tijdsyclus, integratie over de bolus passage, fitting van een gamma variate functie en integratie van de tissue impulse response functie verkregen bij de deconvolutie. Deze laatste methode was het beste voor alle CBF, CBV en SNR waarden.

Gebruikmakend van klinische data werden grote verschillen in de CBF schattingen gevonden tussen verschillende methodes en tussen verschillende weefsels.

Na de vergelijkingen kan geconcludeerd worden dat block-circulant SVD een methode is met veel potentie door het vertraging onafhankelijke gedrag.



---

# Acknowledgements

This master thesis project is the final project of my study biomedical engineering. When I started the study five years ago I was mainly interested in prosthesis and revalidation. I thought this was the perfect combination of technique and the medical world. However, during my study my interests shifted to the physics part of biomedical engineering, specially MRI and radiotherapy. During my internship I combined these two subjects and it confirmed my interests in medical physics.

Working on the master thesis project for almost a year I have experienced a good time and learned a lot of skills. Therefore, I want to pay thanks to some people for their support, aid and shared knowledge during the past time. First of all to Prof. Dr.ir. C.H. Slump who introduced me to the project. His constructive criticism and comments from the initial conception to the end of this work is highly appreciated. Secondly I would like to show my gratitude to Rita Lopes Simões for her patience and advice during the project. I appreciated your fast responses on my questions and our discussions about how to improve my work. Furthermore I really enjoyed the train trips and the conversations during our trips to Nijmegen. I am thankful to Dr. A. van Cappellen van Walsum for willingly accepting to evaluate my Thesis and sit in the examination committee.

Completion of my study would have been all the more difficult without friendship provided by my study colleagues. Therefore I would like to thank Tom Knoop, Renske Koning and José de Zeeuw for the five years of fun, games, wacky gifts, friendship, holidays etc. And of course I really enjoyed the walks during the lunch breaks which were a nice interruption of my study days. I experienced my study in the way that the proverb “Time flies when you are having fun” describes!

I would like to thank especially my family for their continuous support and absolute trust in me. Last but not least, Stefan, words cannot express how wonderful, supportive and loving you have been.

Bianca Maan

Enschede, 22 October 2010



---

# Contents

<b>Abstract</b>	<b>ii</b>
<b>Samenvatting</b>	<b>iv</b>
<b>Acknowledgements</b>	<b>vi</b>
<b>Table of Contents</b>	<b>viii</b>
<b>Glossary</b>	<b>xi</b>
<b>List of Figures</b>	<b>xi</b>
<b>List of Tables</b>	<b>xiii</b>
<b>1 Introduction</b>	<b>1</b>
1.1 Stroke . . . . .	1
1.2 Perfusion imaging . . . . .	2
1.3 Magnetic resonance imaging . . . . .	2
1.3.1 Dynamic susceptibility contrast . . . . .	3
1.4 Project goal . . . . .	4
1.5 Thesis outline . . . . .	5
<b>2 Quantification</b>	<b>7</b>
2.1 Theory . . . . .	7
2.2 Arterial Input Function . . . . .	9
2.3 Deconvolution approaches . . . . .	10
2.3.1 Model-dependent approach . . . . .	10
2.3.2 Model-independent approach . . . . .	11
2.3.3 Statistical approach . . . . .	15
2.3.4 Summary deconvolution approaches . . . . .	15
2.4 Signal integration methods . . . . .	16
2.5 Assumptions . . . . .	17

---

2.5.1	Arterial input function measurement . . . . .	17
2.5.2	Blood-brain barrier . . . . .	18
2.5.3	Linearity concentration . . . . .	18
2.5.4	Hematocrit correction . . . . .	18
2.5.5	Recirculation . . . . .	18
<b>3</b>	<b>Research questions</b>	<b>21</b>
3.1	CBF . . . . .	21
3.2	CBV . . . . .	22
<b>4</b>	<b>Simulations</b>	<b>23</b>
4.1	Simulation of data . . . . .	23
4.1.1	Simulated arterial input function . . . . .	23
4.1.2	Simulated tissue concentration curve . . . . .	24
4.1.3	Add delay and dispersion . . . . .	26
4.1.4	Add Noise . . . . .	27
4.2	Comparisons . . . . .	27
4.2.1	Optimal fixed truncation parameter . . . . .	27
4.2.2	Optimal truncation with and without recirculation . . . . .	30
4.2.3	CBF estimation with different approaches . . . . .	34
4.2.4	CBF estimation with delay or dispersion . . . . .	37
4.2.5	Estimating CBV . . . . .	43
<b>5</b>	<b>Clinical data</b>	<b>47</b>
5.1	Clinical data MRI acquisition . . . . .	47
5.2	Comparison . . . . .	47
<b>6</b>	<b>Conclusions and Recommendations</b>	<b>51</b>
6.1	Research questions . . . . .	51
6.2	Which method is the best? . . . . .	53
6.3	Recommendations . . . . .	54
<b>A</b>	<b>Simplified formulation of gamma variate function</b>	<b>55</b>
<b>B</b>	<b>Graphical User Interface</b>	<b>57</b>
	<b>Bibliography</b>	<b>67</b>

---

# Glossary

---

Abbreviation	Explanation
AIF	Arterial input function
ASL	Arterial spin labelling
CBF	Cerebral blood flow
CBV	Cerebral blood volume
CT	Computed tomography
DSC	Dynamic susceptibility contrast
FT	Fourier transform
GCV	Generalized cross validation
Gd	Gadolinium
GUI	Graphical user interface
LCC	L-curve criterion
MRI	Magnetic resonance imaging
MTT	Mean transit time
PET	Positron emission tomography
PVE	Partial volume effect
RF	Radio frequency
ROI	Region-of-interest
rSVD	Reformulated singular value decomposition
SFTR	Standard form Tikhonov regularization
SNR	Signal-to-noise ratio
SPECT	Single photon emission computed tomography
SVD	Singular value decomposition
TIA	Transient ischemic attack
tSVD	Truncated singular value decomposition
TTP	Time to peak
Xe-CT	Xenon-enhanced computed tomography
A,a,b	Free parameters for gamma variate function
$1/\beta$	Effective mean transit time
$C(t)$	Concentration
$C_t(t)$	Tissue concentration

---

---

$h(t)$	Probability density function of the capillary transit times
$h_{lv}$	Large vessel hematocrit
$h_{sv}$	Small vessel hematocrit
$k$	A proportionality constant
$k_H$	Correction factor for CBV
$N_f$	Number of CBF values used
$M_1$	Method 1
$M_2$	Method 2
$P_{SVD}$	Truncation parameter
$R(t)$	Residue function
$\Delta R_2(t)$	Change in relaxationrate
$\rho$	Brain density
$S(t)$	Signal intensity
$S_0$	Baseline signal intensity
$\sigma$	Standard deviation of baseline signal intensity
TE	Echo time
TR	Repetition time
T1	Longitudinal relaxation time
T2	Transverse relaxation time
T2*	Transverse relaxation time in the presence dephasing
$T_d$	Time delay
$T_{OFFSET}$	Time offset used during rSVD
$t_0$	Time of bolus arrival

---

---

# List of Figures

1.1	Signal intensity time curve . . . . .	3
2.1	Concentration-time curve with recirculation . . . . .	19
4.1	AIF with and without recirculation . . . . .	24
4.2	Three types of residue functions . . . . .	25
4.3	Effect of dispersion on the tissue concentration . . . . .	27
4.4	Mean error curves for tSVD and block-circulant SVD . . . . .	29
4.5	Effect of recirculation on curves without noise . . . . .	31
4.6	Mean error curves for curves with and without recirculation . . . . .	32
4.7	CBF estimates with $P_{SVD}$ of curves without recirculation . . . . .	33
4.8	CBF estimates with tSVD, rSVD and block-circulant SVD . . . . .	35
4.9	CBF estimates with fixed, GCV and LCC $P_{SVD}$ . . . . .	35
4.10	CBF estimates with GCV tSVD and GCV and LCC STFR . . . . .	36
4.11	Effect of delay on curves without noise . . . . .	39
4.12	Effect of delay on curves with noise . . . . .	40
4.13	Effect of dispersion on curves with and without noise . . . . .	41
5.1	Percentage difference tSVD vs. rSVD . . . . .	49
B.1	Parameter input . . . . .	57
B.2	Option selection GUI . . . . .	58
B.3	Comparison GUI . . . . .	59



---

## List of Tables

4.1	Optimal $P_{SVD}$ for tSVD and block-circulant SVD . . . . .	29
4.2	Optimal $P_{SVD}$ for curves with and without recirculation . . . . .	32
4.3	CBV, CBF and MTT values . . . . .	37
4.4	Optimal $P_{SVD}$ for tissue curves . . . . .	38
4.5	CBV estimates using four integration methods . . . . .	44
5.1	Percentage difference between approaches . . . . .	49



---

# Introduction

*This introduction chapter provides background information about perfusion and perfusion imaging. It starts with a short introduction to stroke in section 1.1. This is followed by a description of the currently used imaging methods to detect and quantify brain perfusion in section 1.2. In section 1.4 a formulation of the goal of this thesis project is given. The introduction concludes with an outline of the content of this thesis.*

The circulation of blood through the body is an important process in a living organism. Nutrients are carried in the blood to the tissue and delivered in the tissue capillary bed. The delivery of blood to the capillary bed is called perfusion. When tissue experiences a decrease or absence of perfusion, the tissue can be quickly damaged. The perfusion of the brain is called cerebral perfusion, which is essential to maintain brain function. Stroke is an example of a disease concerning with reduced blood flow and therefore reduced perfusion.

## 1.1 Stroke

Stroke is a type of vascular disease that affects the arteries leading to and within the brain. The blood flow to the brain tissue can be hampered in two ways. The most common kind of stroke, called ischemic stroke, is caused by a clot inside the vessel that blocks the blood flow. The second type, called hemorrhagic stroke, is caused by a rupture of the vessel wall. A briefly interruption of the blood supply is called a transient ischemic attack (TIA).

Hypoperfused tissue can be divided into three compartments. Tissue that will inevitably die (core), tissue that will in principle survive (oligemia), and tissue that may either die or survive (ischemic penumbra) [1]. The final tissue outcome depends on two factors, namely the severity and the duration of the flow reduction. Unless early reperfusion occurs, the volume of the core grows and the amount of penumbra decreases. Reperfusion of tissue can be

achieved using thrombolytic therapy when this is started within 6 hours [2].

There is the intention to perform follow-up studies to investigate the recovery of stroke patients. During follow-up studies very subtle changes should be measurable. Therefore a reliable and accurate perfusion quantification method is needed.

## 1.2 Perfusion imaging

There are a few imaging techniques developed to evaluate brain hemodynamics. The main imaging techniques are positron emission tomography (PET) [3, 4], single photon emission computed tomography (SPECT) [5], Xenon-enhanced computed tomography (Xe-CT) [6, 7], dynamic perfusion computed tomography [8, 9] and magnetic resonance imaging (MRI) [10, 11].

MRI can be divided in two common techniques. One based on arterial spin labeling (ASL) and one based on dynamic susceptibility contrast (DSC). The ASL method is completely non-invasive and uses water in the arterial blood as an endogenous tracer [12], while DSC perfusion MRI makes use of an intravascular injected paramagnetic contrast medium [13].

All these imaging techniques provide information about the current state of the brain. The information is provided in the form of parameters such as cerebral blood flow (CBF), cerebral blood volume (CBV), mean transit time (MTT) and time to peak (TTP). The gold standard for quantitative perfusion imaging is  $H_2^{15}O$  positron emission tomography. This method is frequently used as validation for other new techniques [3, 4, 14]. For clinical purposes, the method has substantial disadvantages, including the need for an arterial catheter to measure the arterial tracer concentration, the application of radioactivity, and the limited availability of PET centers with a cyclotron for the required on-site production of the radionuclide. For follow up studies a less invasive method is essential. This thesis is focused on DSC-MRI because of the disadvantages of PET and the need for another less invasive method for follow up studies. Furthermore DSC-MRI data is more widespread available compared to ASL data.

## 1.3 Magnetic resonance imaging

MRI is a medical imaging technique to visualize the internal structure of the body using the hydrogen atoms in the body. The MRI scanner uses a strong magnetic field to align the nuclear magnetization of hydrogen atoms to the longitudinal direction. With radio frequency (RF) pulses the alignment of the magnetization is altered systematically to the transverse direction. The application of the RF pulse is called excitation. The detectable signal is caused by the protons which return to their original magnetization alignment after the RF pulse is turned off. This process is called relaxation.

The recovery of longitudinal magnetization is caused by a process called T1 recovery. The decay of the transverse magnetization is caused by a process termed T2 decay. T2\* decay is the decay of the signal as a combination of the T2 decay itself combined with the dephasing due to magnetic field inhomogeneities [15]. Inhomogeneities are areas within the magnetic field that do not exactly match the external magnetic field. T1, T2 and T2\* are tissue dependent, therefore anatomical images can be made using the measured time values.

### 1.3.1 Dynamic susceptibility contrast

Perfusion measurements by DSC-MRI utilize dynamic imaging with a repetition time (TR) in the order of seconds to measure the signal changes induced by the tracer in the tissue, as a function of time. Gadolinium (Gd)-based chelates are commonly used as tracer. The tracer injection is usually followed by a saline flush to obtain a short contrast bolus. During the first pass of the bolus through the vessels of the brain, the extraction of contrast agent is zero if the blood-brain barrier is intact [13].

However, the successive images show a signal decay of the spins during the pass of the tracer bolus. This is visible as a drop in the signal intensity curve, see Figure 1.1. When the blood-brain barrier is intact, the tracer is compartmentalized within the vascular space of the brain. The compartmentalization leads to localized regions with differences in the magnetic fields and to gradients in the magnetic field. A shortening of the homogeneous T2 measured with a spin-echo experiment, or T2\* measured with a gradient echo experiment, will arise when the diffusion of water molecules between regions of different fields occurs. This susceptibility process is described in detail by Villringer et al. [16].

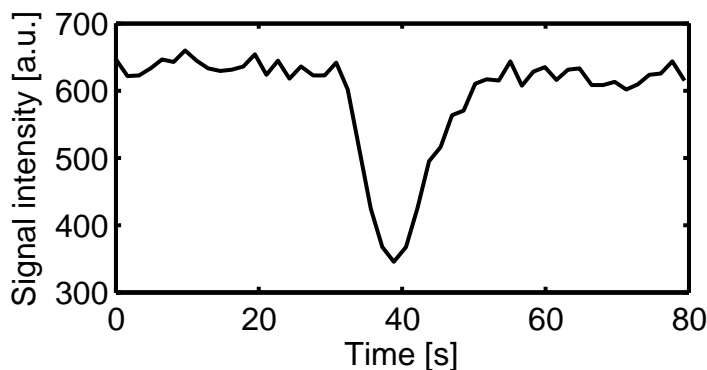


**Figure 1.1:** Signal intensity time curve which shows a signal intensity drop after 30 seconds. This curve is obtained from a single voxel of a clinical dataset.

Besides visualization of the brain hemodynamics, quantitative perfusion values can be obtained as well. Using tracer kinetic models such as the Meier-Zierler model [17], perfusion parameters are derived from the signal-intensity changes in the brain. There are several postprocessing methods to process the data. Variation in quantification has implications for clinical studies, therefore it is important to validate the postprocessing method which is used.

## 1.4 Project goal

Suppose a patient which comes into the emergency room with signs of stroke. After the CT or MRI protocol, stroke is diagnosed. To investigate the recovery of these stroke patients follow up studies are needed. During follow up studies subtle signal differences should be measurable, therefore an accurate and reliable quantification method is necessary. Furthermore a method without radiation is preferable because of the cumulated radiation effects associated with follow up studies. This thesis is focused on quantification of DSC-MRI. However there are multiple quantification methods present for DSC-MRI and it is unknown which method performs best.

The ultimate project goal is the comparison of the commonly used quantification methods used for DSC-MR perfusion imaging. This thesis will be focused on the implementation of the current common used quantification methods. Followed by the comparison of these methods with use of simulated data. Finally the methods are tested using clinical data as well.

This thesis includes the following topics:

- A literature survey of existing quantification methods used for MR perfusion imaging,
- Implementation of the method of choice, i.e. singular value decomposition and signal integration methods in Matlab to obtain perfusion quantities from simulated data and medical perfusion datasets,
- The development of a simple graphical user interface to choose the desired quantification method for clinical datasets, and to make manual selection of the arterial input function possible,
- Performing data simulations to obtain signal curves with known perfusion values. This is followed by a comparison of the known perfusion data with the calculated perfusion data. The research questions are listed in chapter 3.
- Comparison of the methods by calculation of the percentage difference between methods using clinical data.

## 1.5 Thesis outline

The ultimate goal of this thesis is the comparison of the commonly used quantification methods. However, first one method has to be chosen to focus on. Therefore this report starts with a literature survey of the quantification methods. This overview is given in chapter 2. During the literature survey some questions arose about the quantification methods. Therefore chapter 3 gives an overview of the subproblems which are investigated in this thesis. Subsequently in chapter 4 the simulation of MR data is explained followed by different investigations which are performed to answer the subproblems. In addition chapter 5 contains a comparison using clinically obtained MR data of 15 patients. In the conclusion of the report in chapter 6 the research questions which were defined in chapter 3 are answered and some recommendations for further research are made.



---

## Quantification

*Quantitative perfusion measurements may be derived by different postprocessing methods [18]. Most methods demand for user-selected parameters which may lead to variation in quantitative perfusion values. Therefore there are (semi-)automatic methods as well. This chapter provides information about several postprocessing methods which are commonly used. First the theory behind the calculations is explained in section 2.1. In section 2.2 the different approaches to determine the arterial input function (AIF) are mentioned. Section 2.3 gives information about the commonly used deconvolution methods such as singular value decomposition. Section 2.4 provides four methods to integrate the tracer concentration-time curve to calculate CBV. This chapter concludes with a section about the assumptions used during the quantification of perfusion data.*

### 2.1 Theory

As described in subsection 1.3.1, with DSC-MRI a change in signal intensity is visible during the experiment. The perfusion model of Meier-Zierler [17] for non-diffusible tracers uses these signal intensity decay curves. Almost all DSC-MRI perfusion quantification methods are based on this model. The signal intensity of every voxel has to be converted to tracer concentration in order to calculate hemodynamic parameters. Most authors assume that the tissue concentration of the contrast agent is proportional to the change in relaxation rate [18–22]. The relationship between the signal intensity,  $S(t)$ , and the change in relaxation rate,  $\Delta R_2(t)$ , during the passage of the bolus is then given by

$$S(t) = S_0 \exp^{-TE \cdot \Delta R_2(t)}, \quad (2.1)$$

where  $S_0$  is the precontrast signal and  $TE$  the echo time. The concentration  $C(t)$  can then be calculated using

$$C(t) = -\frac{1}{k \cdot TE} \ln \left( \frac{S(t)}{S_0} \right), \quad (2.2)$$

where  $C(t)$  is the contrast agent concentration of the voxel at time  $t$  and  $k$  is a proportionality constant which is unknown [21]. The value of  $k$  is usually set to unity, as it appears as a coactor in both the numerator and dominator in the calculation of cerebral blood volume (CBV) according to Equation 2.4 and therefore drops out of the calculation.

Using the obtained concentration-time curves, perfusion parameters can be calculated per voxel or per region-of-interest (ROI).

CBV is defined as the total volume of blood in a given region of the brain. CBV has units of milliliters of blood per 100 gram of brain tissue (mL/100 g) [23]. By detecting the arterial as well as the total tissue concentration as a function of time during the first pass of the contrast bolus, the CBV can be determined from the ratio of the areas under the tissue and arterial concentration time curves. The arterial concentration time curve is also called arterial input function (AIF), because this curve is the theoretical concentration-time input for all tissue voxels.

A correction factor

$$k_H = \frac{1 - h_{lv}}{\rho(1 - h_{sv})}, \quad (2.3)$$

dependent of the hematocrit values in large ( $h_{lv}$ ) and small ( $h_{sv}$ ) vessels and the brain density ( $\rho$ ) is normally introduced. The incorporation of the hematocrit values into the correction factor is due to the fact that the tracer is distributed in the plasma volume rather than in the whole blood volume [21]. The CBV can be calculated using

$$CBV = k_H \cdot \frac{\int C_t(t) dt}{\int AIF(t) dt}, \quad (2.4)$$

where  $C_t$  and  $AIF$  are the concentration of the contrast material at time  $t$  in the tissue and AIF voxels respectively [13, 21, 22].

The cerebral blood flow (CBF) is defined as the volume of blood moving through a given brain region per unit time, representing the capillary flow in the tissue. CBF has units of milliliters of blood per 100 gram of brain tissue per minute (mL/100 g/min) [23]. To calculate the CBF the residue data  $R(t)$  have to be known.  $R(t)$  is the fraction of the injected tracer still present

in the vasculature at time  $t$  after an in theory infinitely short injection of tracer into the artery.  $R(t)$  can be expressed as

$$R(t) = 1 - \int_0^t h(t)dt, \quad (2.5)$$

with  $h(t)$  the probability density function of the capillary transit times [21, 22]. Theoretically at time zero, the residue function has value one,  $R(0) = 1$ , and if the tracer is not bound to the arterial walls, the contrast will disappear,  $R(\infty) = 0$ . The product  $CBF \cdot R(t)$  is called the tissue impulse response function, as it is the tissue concentration as a result of the infinitely short AIF. However, in fact the AIF will not arrive as an infinitely short bolus but will arrive over a time interval. With other words, the AIF is distributed in time. The tissue concentration time curve becomes the convolution of the tissue impulse response function and the shape of the AIF:

$$\begin{aligned} C_t(t) &= CBF \int_0^t AIF(\tau)R(t - \tau)d\tau \\ &= CBF \cdot R(t) \otimes AIF(t), \end{aligned} \quad (2.6)$$

where  $\otimes$  denotes convolution [13, 21, 22].

When an appropriate AIF is selected, the CBF can be determined by deconvolution. Because  $R(0) = 1$ , theoretically CBF should be equal to the initial height of the tissue impulse response function. However, this is only valid without the presence of delay and dispersion. Therefore in several articles the maximum of  $R(t) \cdot CBF$  is chosen as value for CBF [19, 22, 24] which is used in this report as well.

The mean transit time (MTT) is a measure of the mean time for blood to perfuse a region of tissue [23]. MTT is related to CBF and CBV by the central volume principle:

$$MTT = \frac{CBV}{CBF}. \quad (2.7)$$

## 2.2 Arterial Input Function

Quantification of CBF is done by deconvolution of the tissue concentration curve with the AIF according to Equation 2.6. The most simple approach is to select manually one AIF for the whole brain, this is called global AIF. The manual global AIF is commonly estimated from the signal changes in a major artery, for instance the middle cerebral artery, by selection of one voxel or a region of interest (ROI). There are also methods which are user-assisted; the method identifies candidate AIF locations based on peak

concentration signal intensity and arrival time [25]. Finally it is possible to determine the global AIF automatically as well. For example there is a method based on adaptive thresholding [26] and a method based on the full width at half maximum of the tracer concentration curves [27].

Because the contrast bolus has to travel a distance between the position where the global AIF is measured and the tissue region of interest, bolus delay and dispersion can occur. Therefore local AIF determination is proposed as an AIF which is less prone to delay and dispersion. A smaller vessel closer to the tissue region of interest is used to determine the local AIF.

## 2.3 Deconvolution approaches

To determine CBF and subsequently MTT, deconvolution of the tissue concentration curve with the AIF is required, according to Equation 2.6. The approaches to deconvolve Equation 2.6 can be divided into three main categories: model-dependent, model-independent and statistical approaches.

### 2.3.1 Model-dependent approach

In the model-dependent deconvolution approach, the tissue residue function  $R(t)$  is approximated by an analytical function that models the response of the vascular structure. Assuming a specific shape for  $R(t)$  imposes assumptions on the tissue microvasculature. There are several model-dependent models published.

Larson et al. [28] used an exponential function as shape for the residue function. For this model several assumptions are made, such as: a multiple-inlet, multiple-outlet region of interest can be represented as an equivalent single-inlet, single-outlet system having the same plasma mean transit time. However, when the underlying residue function is non-exponential, an error will be introduced in the CBF estimates [22].

Østergaard et al. [29] presented a modified model which models the vasculature as one major feeding artery in series with 20 small vessels in parallel. The original model is developed to describe major vessel transport as well as microvascular tracer retention of the coronary circulation [30]. The resulting gray-to-white matter CBF ratios, obtained with the modified model, were in good agreement with literature values obtained using PET.

Finally, model-dependent deconvolution can be carried out in the frequency domain as well [31]. Examination of the frequency components of the residue function prior to noise filtering permits the determination of the spectral components that are distorted by noise. The time-domain representation of the exponential shaped residue function should become a Lorentzian function in the frequency domain. Inspection of the less distorted frequency data of the residue function allows the distorted data points to be replaced by values calculated using a model based on the Lorentzian

function. An advantage of frequency domain modeling is that there is no necessity for assumptions regarding the shape of the tissue curves and the AIF. However, this method is model-dependent and cannot be expected to perform equally well for all residue models. In particular for models with significant high-frequency content, such as the box and triangle shaped functions, a more complex frequency-domain model is needed.

### 2.3.2 Model-independent approach

Model-independent deconvolution approaches do not require a priori assumptions regarding the vascular structure [21]. The convolution function is generally unstable, which means that an infinitesimal change in  $C_{Tissue}(t)$  can cause a finite change in  $R(t)$ . There are several techniques which were used to deconvolve Equation 2.6 which mainly differ in the way they moderate the effects of noise in the measurements.

#### Fourier deconvolution approach

In the Fourier transform (FT) approach, the convolution theorem of the FT is utilized. Namely that the transform of two convolved functions equals the product of their individual transforms. In mathematical form the convolution theorem can be written as

$$F \{k \otimes g\} = F \{k\} \cdot F \{g\}, \quad (2.8)$$

where  $F \{ \}$  denotes the discrete FT and  $k$  and  $g$  are functions. According to the convolution theorem, Equation 2.6 can be solved by division in the Fourier domain [21, 32]:

$$\begin{aligned} F \{k_H C(t)\} &= F \{CBF \cdot R(t) \otimes AIF(t)\} \\ &= F \{CBF \cdot R(t)\} \cdot F \{AIF(t)\} \\ CBF \cdot R(t) &= F^{-1} \left\{ \frac{F \{k_H C(t)\}}{F \{AIF(t)\}} \right\}, \end{aligned} \quad (2.9)$$

where  $F^{-1} \{ \}$  denotes the inverse discrete FT.

In this form, the deconvolution approach is very sensitive to noise. However, the frequency representation of the concentration curves contain noise at high frequencies and the physiological signal at low frequencies. This separation between data and noise makes it possible to use a filter to attenuate the noise and retain the physiological data. A Wiener filter is a commonly used filter to obtain the CBF [27, 32]. Smith et al. [33] used the FT deconvolution together with fitting of a gamma-variate function to the concentration data before deconvolution. The use of a gamma-variate function to

remove the recirculation signal is explained in section 2.5.5. Wirestam et al. [34] published two FT approaches, one with gamma-variate fitting to the concentration data of every voxel, and one with a low-pass Hanning filter without gamma-variate fitting. Sakoglu et al. [35] reported a method to find the optimal filter by minimizing the mean-squared error (MSE) between the noiseless and noisy scaled residue function. They found that the technique was stable at low noise levels, but that it underestimated the CBF under moderate noise conditions. The shaped filter function was also found to be sensitive to distortion of the AIF.

### Algebraic approach

In the algebraic approach, Equation 2.6 is rewritten into a matrix equation. Assuming that tissue and arterial concentrations are measured at equidistant time points  $t_1, t_2, t_3, \dots, t_N$ , the convolution theorem can be approximated by a matrix equation [13, 21, 22]:

$$\begin{aligned} C_t(t_j) &= CBF \int_0^{t_j} AIF(\tau)R(t - \tau)d\tau \\ &\approx CBF\Delta t \sum_{i=0}^j AIF(t_i)R(t_j - t_i), \end{aligned} \quad (2.10)$$

where  $C_t(t_j)$  denotes the tissue concentration at time  $t_j$ . Equation 2.10 can also be written in matrix form as

$$\begin{pmatrix} C_t(t_1) \\ C_t(t_2) \\ \dots \\ C_t(t_N) \end{pmatrix} = CBF \cdot \Delta t \begin{pmatrix} AIF(t_1) & 0 & \dots & 0 \\ AIF(t_2) & AIF(t_1) & \dots & 0 \\ \dots & \dots & \ddots & \dots \\ AIF(t_N) & AIF(t_{N-1}) & \dots & AIF(t_1) \end{pmatrix} \cdot \begin{pmatrix} R(t_1) \\ R(t_2) \\ \dots \\ R(t_N) \end{pmatrix}, \quad (2.11)$$

which can be solved iteratively for the elements of  $R(t_j)$ . The AIF matrix is a lower triangular matrix and  $\Delta t$  represents the TR. If the rows of the AIF data matrix are close to being linear combinations of each other, then the matrix is singular and inversion cannot be performed [21].

The technique described above assumes that arterial and tissue concentrations are constant between measurements. However, in dynamic MR imaging, both concentrations are expected to show little variation within the temporal resolution of the measurements. The constancy of these concentrations between measurements is thus a poor approximation. Therefore Østergaard et al. [22] introduced a modification of the AIF matrix in Equation 2.11 which assumed that AIF and  $R(t)$  both vary linearly with time. The elements of the AIF matrix become

$$a_{ij} = \begin{cases} \Delta t(AIF(t_{i-j-1}) + 4AIF(t_{i-j}) + AIF(t_{i-j+1}))/6 & 0 \leq j \leq i \\ 0 & \text{else.} \end{cases} \quad (2.12)$$

To obtain a stable solution of Equation 2.11, noise has to be suppressed. Knutsson et al. [21] and Østergaard et al. [22] give a description how to use singular value decomposition (SVD) to calculate CBF. SVD is a factorization method which is used widely in linear inverse problems. With SVD the pseudoinverse of the AIF matrix can be calculated. Using SVD the AIF data can be decomposed into three matrices:

$$\mathbf{AIF} = \mathbf{U} \cdot \begin{pmatrix} w_1 & 0 & \dots & \dots & 0 \\ 0 & w_2 & \dots & \dots & 0 \\ 0 & 0 & \dots & \dots & 0 \\ \dots & \dots & \dots & \dots & \dots \\ 0 & 0 & \dots & \dots & w_N \end{pmatrix} \cdot \mathbf{V}^T = \mathbf{U} \cdot \mathbf{W} \cdot \mathbf{V}^T \quad (2.13)$$

where  $\mathbf{U}$  and  $\mathbf{V}$  are orthogonal matrices, so their inverses are equal to their transposes. The inverse of  $\mathbf{AIF}$  can then be written as [36]:

$$\mathbf{AIF}^{-1} = \mathbf{V} \cdot \left[ \text{diag} \left( \frac{1}{w_j} \right) \right] \cdot \mathbf{U}^T. \quad (2.14)$$

The tissue impulse response function,  $CBF \cdot R(t)$ , can thus be calculated as:

$$CBF \cdot R(t) = \mathbf{V} \cdot \left[ \text{diag} \left( \frac{1}{w_j} \right) \right] \cdot (\mathbf{U}^T k_H C(t)). \quad (2.15)$$

The smallest singular values in matrix  $\mathbf{W}$  correspond to high frequencies. In an actual calculation of the SVD, even singular values that theoretically should be zero will show up as extremely small but non-zero values in the matrix  $\mathbf{W}$ . This is caused by round-off errors and noise in the data. A direct application of the calculated matrix  $\mathbf{W}$  will produce large oscillations in the final solution. Regularization refers to mathematical methods which improve the stability in such problems.

One straightforward method is referred to as truncated SVD (tSVD) [37, 38]. This method treats all singular values below a certain threshold, also called truncation parameter ( $P_{SVD}$ ), as exact zeros. Using this method the effects of noise are reduced. However, a high threshold can lead to underestimation of the CBF [39]. The resulting found  $R(t)$  can be shown to be the best possible solution in a least squared sense [36]. It is possible to use a fixed  $P_{SVD}$  for all curves. However there are methods to calculate the  $P_{SVD}$  for every curve separately as well. Generalized cross validation (GCV) and L-curve criterion (LCC) are well-known methods for this voxel based purpose [37].

An alternative regularization method is known as standard form Tikhonov regularization (SFTR). The solution of this method can be written by

replacing  $diag[1/w_j]$  with  $diag[w_j/(w_j^2 + P_{SVD}^2)]$  [38]. SFTR performs a 'smooth' truncation of the singular values. GCV or LCC are frequently used methods for selection of the optimal  $P_{SVD}$  for SFTR.

The standard SVD approach as described above is delay sensitive. Nowadays there are new, slightly modified, SVD approaches such as reformulated SVD (rSVD) [40] and block-circulant SVD [19] which are reported to be delay insensitive.

With rSVD the first nonzero estimate of the residue function is obtained at time  $t = T_{OFFSET}$ . The parameter  $T_{OFFSET}$  must represent a time that is larger than the absolute value of the largest expected experimental negative arrival time plus the duration of signal distortions introduced when discarding singular values. It was found that  $T_{OFFSET} = -n \cdot TR$  with  $n = 40$  and  $TR \leq 0.25$  s gives practical equivalence CBF estimates of rSVD compared with FT. With discrete  $C_t(t)$  data, this method is computationally equal to shifting the experimental  $C_t(t)$  values by  $n$  samples. After this computational time shift the SVD approach is equal to the previously described SVD approach.

With block-circulant SVD the same basic SVD approach is used. In this case both the AIF matrix and the  $C_t(t)$  vector are changed. By zero-padding the N-points AIF-time and the tissue concentration-time curve to length L, where  $L \geq 2N$ , time aliasing can be avoided. Secondly, the matrix AIF is changed.

$$a_{ij}^{\#} = \begin{cases} a_{i,j} & 0 \leq j \leq i \\ a_{L+i,j,0} & else. \end{cases} \quad (2.16)$$

Using this AIF matrix and the zero-padded tissue concentration curve, the standard SVD approach can be followed.

### Optimal choice

The optimal choice of some transform and algebraic approaches was studied using Monte Carlo simulations [22]. The FT approach was found to underestimate the CBF with short MTT. Calculating the CBF of two regions with equal CBF but different CBV gives two different answers. The region with the highest CBV, and therefore the highest MTT, will appear to have a higher CBF. The FT approach is thus misleading in evaluating states of high flow and short MTT unless the sampling rate can be improved relative to the MTTs. Furthermore, when an unmodified Wiener filter is used, the mean square error over the whole time range is minimized. However, the first values of the impulse response function are of importance. A modified Wiener filter [32] or Hanning filter will compensate these filter problems. Finally, an advantage of the FT approach is the insensitivity to delay of the AIF.

The SVD approach showed a good ability to reproduce flow with good accuracy independent of the underlying vascular structure and volume. With decreasing SNR, the shape of the residue function becomes less detailed. However, the initial and maximum point on the residue curves still remains constant. At a SNR of below 50-100, the noise is too large to yield qualitative information. The SVD approach has some drawbacks as well. First, the results of the deconvolution are dependent of the chosen truncation value [39] and secondly, the deconvolution is sensitive to delay and dispersion [41]. However, rSVD and block-circulant SVD are reported to be delay insensitive [40].

There is not one optimal approach; all have their own advantages and disadvantages. However, SVD and especially truncated SVD is the most well accepted method.

### 2.3.3 Statistical approach

The residue function can be approximated using statistical approaches as well. Statistical approaches do not require a priori assumptions regarding the vascular structure. Vonken et al. [42] used an iterative maximum likelihood expectation maximization algorithm (ML-EM) which is based on the expectation maximization framework described by Dempster et al. [43]. The ML-EM algorithm makes an estimate of the tissue response function ( $CBF \cdot R(t)$ ), convolves it with the AIF and then compares the outcome with the measured tissue concentration curves to correct the estimate. They reported that the method is less sensitive to noise than other methods. Willats et al. [44] proposed a modified ML-EM method that minimized the artifacts associated with deconvolution by using a pointwise termination approach. With this method, the sharp edges of a non-dispersed delayed concentration curve can be reconstructed.

It is also possible to obtain the residue function using a Gaussian process [45]. This method has the smoothness of the impulse response function incorporated as a constraint.

Zanderigo et al. [46] proposed a deconvolution method based on non-linear stochastic regularization (NSR). They reported that NSR performs better than SVD and SFTR in reconstructing both the peak value and the residue function, specially when dispersion was considered.

### 2.3.4 Summary deconvolution approaches

Deconvolution of the tissue concentration curve with the AIF is an important step in the quantification processing of perfusion data. There are model-dependent, model-independent and statistical approaches. The model-dependent approaches require a priori knowledge about the vasculature. Exponential decrease has been proposed as a general model for tissue

residue functions. However, this is wrong for more complicated vascular structures and plug flow. A wrong assumption can introduce large errors in the calculated residue function.

There are two well-known model-independent deconvolution approaches, namely Fourier transform (FT) and singular value decomposition (SVD). The FT uses the convolution theorem to calculate the residue function while the SVD method uses matrix equations. Both approaches have advantages and disadvantages. For example, FT is insensitive to delay of the AIF while this approach underestimates CBF in voxels with high CBV and short MTT. SVD is independent of the vasculature and CBV, but is dependent on the cut-off value used during the deconvolution. Truncated SVD, SVD with a certain threshold for the diagonal values of matrix  $\mathbf{W}$  (Equation 2.13), is the most used deconvolution method. This approach is less sensitive to noise.

For statistical deconvolution approaches, no a priori assumption about the vascular structure are needed. This is an advantage for statistical approaches. Furthermore NSR is reported to be independent of bolus dispersion.

This thesis is focused on SVD deconvolution approaches because this is the most used method in DSC-MRI quantification. Comparison of different SVD approaches has not been done before to the best of our knowledge. Furthermore different investigations are done with different types of SVD approaches which makes it difficult to compare them. Therefore it is important to know which approach performs best.

## 2.4 Signal integration methods

In general, the determination of CBV involves the integration of the tissue concentration-time curve either on a pixel-by-pixel or a ROI basis. A typical arterial and tissue concentration curve contains two peaks. This is explained in more detail in section 2.5

There are several possibilities to perform the integration. The easiest method is the numerical integration of the whole concentration-time curve, i.e. from the arrival of the bolus till the end of the acquisition. This method includes the recirculation, therefore it does not yield absolute CBV. However, Kosoir et al. [24] claim that the calculations of CBV are independent of the recirculation.

The second method, which is frequently used, is the integration of the concentration-time curve from the arrival time of the contrast bolus till the minimum of the curve between the first pass and the recirculation. With this method the recirculation is removed from the CBV calculations. Usually the integration boundaries are determined on the signal-intensity curve which is based on the mean signal-intensity of all the brain voxels. This means that all voxels are integrated with the same boundaries. Therefore it is likely to

underestimate CBV in areas with prolonged MTT where the first pass is broadened, extending beyond the upper integration boundary.

Another method which is frequently used in perfusion imaging is fitting a gamma variate function to the concentration-time curve. This procedure is explained in section 2.5.5. Finally, CBV can be derived by integration of the tissue impulse response function [32, 47].

Perkiö et al. [18] evaluated the use of the four postprocessing methods for determination of CBV and MTT. They concluded that for relative CBV and MTT measurements numerical integration over the whole time curve is optimal in terms of computational efficiency, signal-to-noise ratio (SNR), and accuracy of relative values. For absolute CBV and MTT measurements, the area under the SVD deconvolved tissue curve provides the most accurate estimates.

## 2.5 Assumptions

Although deconvolution of the concentration-time curves could in theory provide accurate and reliable perfusion parameters, there are several assumptions in the tracer kinetic model used in the quantification of perfusion. These assumptions may be invalid in cerebral ischemia. In this section the most important assumptions are mentioned.

### 2.5.1 Arterial input function measurement

As described in section 2.2, the AIF is in practice manually selected in a major artery with the assumption that this represents the exact input to the tissue. However, with selection of one incorrect global AIF the results of all voxels will be influenced.

Firstly, delay and dispersion of the bolus from the location of AIF estimation to the tissue can cause an error in the quantification. This error could vary between regions because of differences in the amount of delay and dispersion between the tissue regions in the brain [48]. The rSVD and block-circulant SVD approaches are insensitive to delay, however SVD approaches are still sensitive to dispersion.

Secondly, due to the limited spatial resolution of a typical DSC-MRI experiment, measurements of the AIF are likely to include signal components from tissue surrounding the vessel. This is called partial volume effect (PVE). Chen et al. [49] reported that PVE can induce significant CBF estimation biases. One approach to minimize the effects of PVE is scaling of the estimated AIF. For example this can be done using the venous output function measured from the sagittal sinus [50]. Selecting the AIF in large vessels minimize the PVE effects, however the amount of delay and dispersion can be increased due to the longer distance between the AIF location and the tissue voxels.

Furthermore the AIF is dependent of the sequence that is used. While gradient-echo is sensitive to the total vascular space, spin echo is more specific to the capillary bed. As a consequence of the latter, it has been suggested that spin-echo sequences cannot provide an absolute measurement of the AIF [50].

### 2.5.2 Blood-brain barrier

DSC-MRI quantification methods rely on the assumption that the blood-brain barrier is intact. When the blood-brain barrier is damaged, the Gd chelate will be transported into the extravascular space. As a consequence the tracer is not compartmentalized anymore, leading to a reduction in the T2/T2\* relaxation in the extravascular tissue which affects the signal-intensity time course [51]. This can cause an error in the final CBF and CBV values.

### 2.5.3 Linearity concentration

The concentration of the contrast tracer, in both the tissue and the AIF, is assumed to be linearly proportional to the change in relaxation rate. Furthermore the proportionality constant has to be independent of tissue type. However, the proportionality constant has been shown to be tissue dependent [52]. This dependency can cause an error in the estimated values compared between the different tissue types.

### 2.5.4 Hematocrit correction

In the absolute quantification of CBV and CBF, a correction factor based on the brain density and the hematocrit values of the large and small vessels is included in the calculations (Equation 2.3). It is known that hematocrit levels in the tissue can increase during acute ischemia, and decreased levels have been reported during chronic carotid artery stenosis. A local change in hematocrit levels will affect the measurements [48].

### 2.5.5 Recirculation

A typical vessel and tissue concentration curve contains two peaks. First a large peak corresponding to the first pass of the contrast bolus and secondly a smaller peak corresponding to the recirculation of the contrast material. Figure 2.1 shows an example of a theoretical AIF with recirculation. In the AIF the separation of the two peaks can be clearly visible, however in tissue concentration curves the second peak coincides most of the time with the down slope of the first pass.

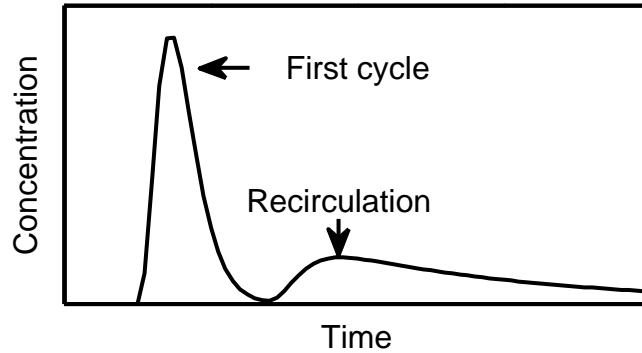


**Figure 2.1:** *Concentration-time curve with recirculation.*

Most authors assume that the tracer recirculation has to be removed to derive CBF and CBF [14, 31, 53]. One well-known method to remove the tracer recirculation is fitting a gamma variate function to the first pass of the concentration time curve. This approach is explained in section 2.5.5. Recently, Kosior et al. [24] reported that it is a common misconception that the tracer recirculation must be removed. Using simulations they showed that the tracer recirculation does not have impact on the estimation of CBF.

### Fitting a gamma variate function

The recirculation can be eliminated from the signal by using a gamma variate function. This function is fitted to the first pass of the concentration-time curve. The gamma variate function is usually expressed as

$$y(t) = A(t - t_0)^a e^{-(t-t_0)/b}, \quad (2.17)$$

which is valid for  $t > t_0$ , where  $t$  is the time,  $t_0$  is the arrival time and  $A$ ,  $a$  and  $b$  are free parameters. The nonlinear methods of fitting the gamma variate function to the observed concentration-time curves are computationally intensive because it has to be done for all voxels separately. In addition, the free parameters has to be defined beforehand to perform a fit. There is also a simplified formulation of the gamma variate function which uses a least-squares linear algorithm of fitting in the first-pass phase of the curve [54]. This method is explained in more detail in Appendix A.



---

## Research questions

*During the literature study several questions arose about the quantification methods. This chapter provides a list of questions which are answered in this thesis. First in section 3.1 the research question involving the calculation of CBF are mentioned. This is followed by the questions related to the CBV calculations in section 3.2.*

### 3.1 CBF

- **Deconvolution using fixed  $P_{SVD}$**

One frequently used regularization approach is the use of a fixed truncation parameter,  $P_{SVD}$ . However the estimated CBF is dependent on the  $P_{SVD}$ . A large  $P_{SVD}$  causes underestimation of CBF while a small  $P_{SVD}$  can overestimate CBF because it does not reduce the noise enough. For SNR 100 and 20 optimal  $P_{SVD}$  values of 20 and 4% respectively using tSVD are reported [19, 22]. Using block-circulant SVD these values are 10 and 5% respectively [19]. Other studies use these values, therefore it is interesting to reproduce this investigation to validate these findings. The following research question is formulated:

*Which  $P_{SVD}$  values are optimal using tSVD and block-circulant SVD with SNR 100 and 20?*

- **Tracer recirculation**

In several studies [14, 31, 53], tracer recirculation is removed before deconvolution. However this is a common misconception according to Kosior et al. [24]. They show that it is unnecessary to remove tracer recirculation from bolus-tracking data to derive CBF and CBV. However they investigated this using tracer concentration curves without noise. This leads to the following question:

*Is CBF immune to tracer recirculation in the presence of noise as well?*

○ **Estimating CBF without delay and dispersion**

tSVD, rSVD and block-circulant SVD are slightly different approaches. So their performance in estimating CBF may be different as well. Furthermore regularization can be applied using a fixed  $P_{SVD}$  or using a  $P_{SVD}$  determined per voxel using GCV and LCC. Furthermore SFTR can be used to perform a smooth truncation.

*Which deconvolution method, tSVD, rSVD or block-circulant SVD, provides the best CBF estimations? And which method to determine the  $P_{SVD}$  performs best?*

○ **Estimating CBF in the presence of delay and dispersion**

Delay and dispersion are two effects which can be present in tracer concentration-time curves, especially in hypoperfused tissue. Therefore it is important to investigate which method performs best in the presence of delay and dispersion.

*Which deconvolution method, tSVD, rSVD or block-circulant SVD, provides the best CBF estimations in the presence of delay? And which method in the presence of dispersion?*

## 3.2 CBV

○ **Estimating CBV without delay and dispersion**

There are multiple methods to calculate CBV. For example the tissue concentration curves and the AIF can be integrated directly using the discrete data. This can be done with different integration boundaries, namely the start of the first pass till the end of the acquisition, or till the end of the first pass. Furthermore, the area under the curves can be estimated using a gamma variate fit. With this fit the recirculation part of the concentration curves is eliminated from the CBV calculations. Finally it is possible to integrate the area under the tissue impulse response function which is obtained by deconvolution.

*Which of these four CBV calculation method provides the best CBV estimations?*

---

# Simulations

*Validation of different postprocessing methods can be done using phantom measurements or using simulated data. The latter is used during this research project. The performance of different postprocessing methods can be investigated using Monte Carlo simulations. The data simulation is described in section 4.1. Subsequently section 4.2 gives an overview of the comparisons which are made. For each comparison the methods, results and discussion are described separately.*

## 4.1 Simulation of data

To compare different postprocessing methods, tissue and arterial concentration curves are needed. During the simulations first the arterial concentration curve, i.e. the AIF, is simulated. Using this AIF the tissue concentration curves can be calculated.

### 4.1.1 Simulated arterial input function

An AIF is simulated using a gamma-variate function, with a shape and size that is obtained using a standard bolus injection scheme [22]. The analytical expression of the AIF is

$$AIF(t) = \begin{cases} 0 & t \leq t_0 \\ A(t - t_0)^a \cdot e^{-(t-t_0)/b} & t > t_0 \end{cases} \quad (4.1)$$

with  $A$  a scaling factor,  $t_0$  the contrast arrival time and  $a$  and  $b$  are shape parameters which depend on the vasculature and blood flow. Parameters used in this study where  $A = 1$ ,  $t_0 = 20$  s,  $a = 3.0$  and  $b = 1.5$  s. The repetition time (TR) is 1 second for all simulated datasets. Subsequently

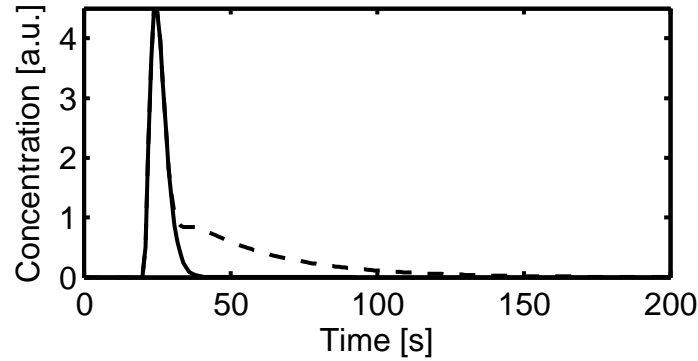


**Figure 4.1:** *AIF with and without recirculation. The solid line shows the gamma variate function, the dashed line describes the gamma variate function including recirculation.*

the recirculation is calculated by convolving the obtained AIF, with an additional delay of 8 seconds, with an exponential with a time constant of 30 seconds. Figure 4.1 shows an AIF with and an AIF without recirculation.

#### 4.1.2 Simulated tissue concentration curve

To investigate the performance of different deconvolution methods, tissue curves produced with known residue functions  $R(t)$  are used. There are three different models for the tissue residue function used in the simulations, as done by Østergaard et al. [22]:

1. *Box shaped residue function.* This residue function is given by

$$R(t) = \begin{cases} 0 & t < 0 \\ 1 & 0 \leq t \leq MTT \\ 0 & t > MTT. \end{cases} \quad (4.2)$$

This function describes a vascular bed with 'plug flow' where the capillaries are parallel with equal length and mean transit times.

2. *Triangular shaped residue function.* This residue function is given by

$$R(t) = \begin{cases} 0 & t < 0 \\ 1 - \frac{t}{2 \cdot MTT} & 0 \leq t \leq 2 \cdot MTT \\ 0 & t > 2 \cdot MTT. \end{cases} \quad (4.3)$$

This function describes an intermediate model between a single, well-mixed compartment and a model of parallel capillaries with equal transit times ('plug flow') [39].

3. *Exponential residue function.* This residue function is given by

$$R(t) = \begin{cases} 0 & t < 0 \\ e^{-\frac{t}{MTT}} & 0 \leq t. \end{cases} \quad (4.4)$$

This function describes the vasculature as one single, well-mixed compartment.

Figure 4.2 shows the graphs of the three types of residue functions.

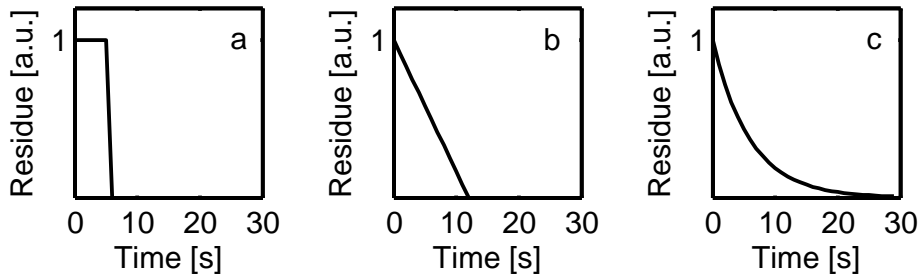


**Figure 4.2:** Three types of residue functions with  $MTT = 6s$ . a) Box shaped residue function, b) Triangle shaped residue function, c) Exponential residue function. For clarity only the first 30 seconds are depicted.

The tissue concentration curves are calculated using Equation 2.6. With different values for CBF, CBV and MTT different tissue curves can be obtained. The values used for each comparison are mentioned in section 4.2.

The obtained concentration-time curves are converted to signal intensity-time curves using

$$S(t) = S_0 e^{-k \cdot C(t) \cdot TE} \quad (4.5)$$

which is equivalent to Equation 2.1 including a proportionality factor  $k$  which is used to match a typical peak drop in signal intensity. For all simulations, a proportionality factor  $k$  is selected that resulted in a 40% peak signal drop at a flow rate of 60ml/100g/min and  $CBV = 4\%$  using an exponential residue function. These values correspond to values typically found in human gray matter [22, 41]. Furthermore  $S_0$  depends on scanner hardware and software and is entirely arbitrary. During the simulations  $S_0 = 100$  and  $TE = 30$  ms are used. The signal intensity-time curve for the AIF is similarly modeled as  $S(t)$ , except that AIF is substituted for  $C(t)$ . The proportionality constant,  $k$ , is in this case selected to generate a peak signal drop of 60% as done by Wu et al. [19]. To determine absolute flow values at the end of the calculations, the calculated CBF values are rescaled by the  $k$ -factors used.

### 4.1.3 Add delay and dispersion

As mentioned by Calamante et al. [41], since it is in practice not possible to measure the true AIF for every pixel, this is usually estimated from a major vessel such as the middle cerebral artery by selection of one voxel or a ROI. In subsequent calculations one single AIF is used for the whole brain. The estimated AIF may undergo delay and/or dispersion between the position of AIF recording and the position of the tissue. To simulate delay and dispersion, the model described by Calamante et al. [41] is used. This model will be explained briefly.

The effect of dispersion can be described mathematically as a convolution with a vascular transport function  $h^*(t)$  from the site of measurement, the estimated AIF, to the given pixel, the true AIF:

$$AIF(t) = AIF^{(est)}(t) \otimes h^*(t). \quad (4.6)$$

The tissue concentration then becomes

$$\begin{aligned} C(t) &= CBF \cdot AIF(t) \otimes R(t) = CBF \cdot \left( AIF^{(est)}(t) \otimes h^*(t) \right) \otimes R(t) \\ &= CBF \cdot AIF^{(est)}(t) \otimes (h^*(t) \otimes R(t)). \end{aligned} \quad (4.7)$$

Equation 4.7 shows that simulation of dispersion is equivalent to a convolution of the estimated AIF with an effective residue function,  $R^{(eff)} = h^* \otimes R$ . Calamante et al. [41] reported

$$h^*(t) = \beta \cdot e^{-\beta t} \quad (4.8)$$

as a first approximation for the vascular transport function. With this approximation the assumption as a well-mixed compartment is used for the vasculature.  $1/\beta$  corresponds to the effective MTT from the position of AIF recording to the position of the tissue.

Using this model, the effective residue function can be written as

$$R^{(eff)}(t) = \frac{\beta}{\left(\frac{1}{MTT} - \beta\right)} \cdot \left( e^{-\beta t} - e^{-t/MTT} \right). \quad (4.9)$$

This effective residue function is used instead of the previously described residue function to simulate dispersion. Figure 4.3 shows one tissue concentration-time curve without dispersion and one curve with dispersion using  $1/\beta = 6s$ . A clear spread of the peak and decrease of its height can be seen. In addition, the peak of the curves shifts.

Subsequently delay of the curve can be simulated by shifting the obtained tissue curve with a time delay,  $t_d$ .

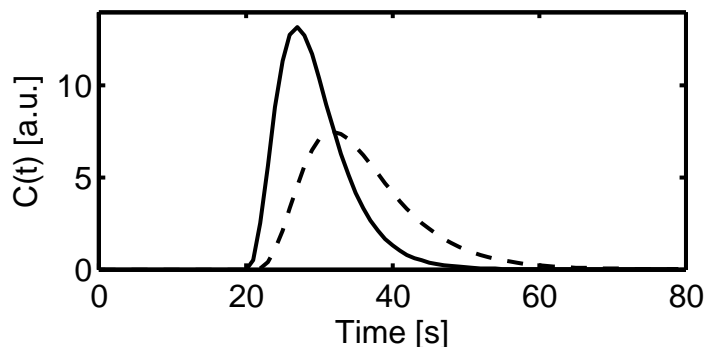


**Figure 4.3:** *Effect of dispersion on the tissue concentration using  $CBV = 4\text{ml}/100\text{g}$  with  $CBF = 60\text{ml}/100\text{g}/\text{min}$ . The solid line represents the nondispersed case, while the dashed line shows the concentration for  $1/\beta = 6\text{s}$ .*

#### 4.1.4 Add Noise

The obtained signal intensity-time curves are expanded into 1024 copies. Zero-mean random Gaussian noise is added to each curve to generate 1024 different curves. With the Gaussian noise, curves with different signal to noise ratios (SNR) are obtained. The SNR is given by

$$SNR = \frac{S_0}{\sigma} \quad (4.10)$$

where  $S_0$  denotes the baseline signal intensity and  $\sigma$  the standard deviation of the noise at the baseline signal intensity. Two different noise values are chosen with standard deviations 1 and 5, corresponding to SNRs of 100 and 20 respectively, based on literature [19].

Although the noise in MR magnitude images is characterized by a Rician distribution, it has been shown to be well approximated by a Gaussian distribution for  $SNR > 2$  [55].

## 4.2 Comparisons

Using the simulated data described in section 4.1 the performance of different deconvolution approaches and different CBV calculation methods are investigated. In this section, the methods of the different investigations together with the corresponding results and discussion are described.

### 4.2.1 Optimal fixed truncation parameter

As described in section 2.3.2 one straightforward method for the regularization of ill-posed problems is truncation of the singular values using a fixed

threshold,  $P_{SVD}$ . Wu et al. [19] reported optimal  $P_{SVD}$ 's for tSVD and block-circulant SVD with SNR 20 and 100. In this research the optimal  $P_{SVD}$  is calculated for tSVD and block-circulant SVD using the method described by Wu et al. [19] to validate these findings.

### Method

For this investigation all three types (box, triangle and exponential) of residue functions, as described in subsection 4.1.2, are used. All curves are created without recirculation. The data is simulated over a time range of 200 seconds with TE = 65 ms to keep the parameters equal to the parameters used in the article by Wu et al. [19]. CBV is either 4% or 2%. For CBV 4%, flow values are varied between 10-70 mL/100 g/min in 10 mL/100 g/min increments. For CBV = 2%, flows are evaluated from 5-35 mL/100 g/min using 5 mL/100 g/min increments in order to maintain the same range of MTT values as for CBV = 4%. MTT is calculated from the central volume theorem (Eq. 2.7). Noise is added to obtain curves with SNR 20 and 100, as described in subsection 4.1.4. The  $P_{SVD}$  is varied between 0.1% and 90%.

For each  $P_{SVD}$  the error at each of the 1024 iterations  $t$  ( $E_t$ ) is calculated as

$$E_t = \frac{1}{N_f} \cdot \sum_1^{N_f} |F - F'|, \quad (4.11)$$

where  $F$  is the true CBF value,  $F'$  is the estimated CBF value and  $N_f$  is the number of simulated CBF values. In this case  $N_f = 7$ , seven CBF values are used for each CBV. The optimal  $P_{SVD}$  is determined as the value that minimized the averaged  $E_t$  simultaneously over all assumed residue functions, all CBV values and all 1024 iterations assuming zero time delay and no dispersion.

### Result

In total for each SNR and each SVD approach, six mean error-curves are calculated using Equation 4.11. Namely for three types of residue functions and two CBV values. The mean of these six curves is calculated. In this way, one error curve per SNR and SVD approach is obtained. These mean error curves are depicted in Figure 4.4. The minimum of each mean error curve represents the optimal  $P_{SVD}$  for the given SNR and SVD approach.

The optimal  $P_{SVD}$ 's for truncated and block-circulant SVD are listed in Table 4.1. The  $P_{SVD}$ 's for block-circulant SVD are lower in comparison with the values found for tSVD. As could be expected, the values are lower for SNR 100 than for SNR 20.

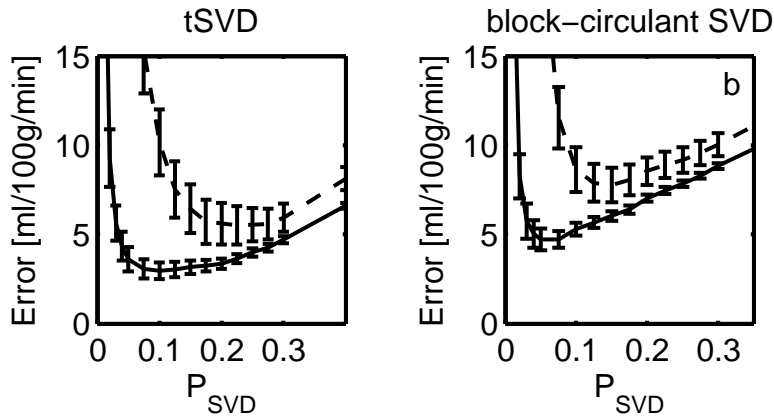


**Figure 4.4:** Mean error curves over three types of residue functions, two CBV values and 1024 iterations. a) shows the curves calculated using tSVD. b) shows the curves using block-circulant SVD. The dashed lines represent SNR 20, the solid lines represent SNR 100. For clarity, the errorbars represent 2SD.

SNR	tSVD	block-circulant SVD
20	22.5%	15%
100	10%	5%

**Table 4.1:** Optimal  $P_{SVD}$  values using tSVD and block-circulant SVD. Optimal value is obtained using tissue concentration-time curves made with box, triangle and exponential residue functions.

## Discussion

Figure 4.4 shows the mean error curves over three types of residue functions and two CBV values. The location of the minimum of the error curve corresponds to the optimal  $P_{SVD}$ . For  $P_{SVD}$ 's below the optimal  $P_{SVD}$  the noise is not suppressed enough and will cause an overestimation of the CBF estimates. After the minimum is reached, the error increases for high  $P_{SVD}$ 's. With a large  $P_{SVD}$ , more singular values of the AIF matrix are removed and therefore the residue function will contain less frequencies. This removal of the singular values causes underestimation of the residue function and the CBF estimates. Because of this under and overestimation by selection of a improper  $P_{SVD}$  errors in absolute CBF estimates can occur. These errors can influence clinical decisions and the interpretation of follow-up studies.

The optimal  $P_{SVD}$ 's found in this research study are not exactly equal to the values reported by Wu et al. [19]. For curves with SNR 20 Wu et al. reported 20% and 10% for tSVD and block-circulant SVD respectively while the results of this thesis are 22.5% and 15%. For curves with SNR 100

combined with the block-circulant approach equal  $P_{SVD}$  is found, namely 5%. However, for curves with SNR 20 combined with the tSVD approach a large difference in optimal  $P_{SVD}$  is found. The optimal  $P_{SVD}$  of 10% is more than twice the  $P_{SVD}$  of Wu et al. namely 4%. Knutsson et al. [20] investigated the influence of the  $P_{SVD}$  as well. They reported a  $P_{SVD}$  of 10% for curves with an SNR higher than 70 which is comparable to the  $P_{SVD}$  reported in this thesis.

When articles mention a optimal  $P_{SVD}$ , it is reported as one fixed value as optimum. However, Figure 4.4 shows a range of values which give almost the same error. Therefore for some deconvolution methods it is possible to select a  $P_{SVD}$  within a range of values. For example, for tSVD and curves with SNR 20, an optimal  $P_{SVD}$  can be selected between 20% and 25%. However, this is not valid for all deconvolution approaches. The error curves of block-circulant SVD for a specific tissue concentration curve has a narrower peak drop than error curves of tSVD. Because the optimal  $P_{SVD}$  is dependent on the value of CBF [39], the location of the peak drop shifts with a change in CBF. Therefore the mean error over all CBF and CBV curves is higher and the range of possible  $P_{SVD}$  values is smaller.

Finally, as could be expected, there is a difference in optimal  $P_{SVD}$  between the different SNR values. The truncation of the eigenvalues is performed to suppress the noise in the obtained residue function. However, when the original signals contain less noise, the amount of suppression can be reduced, i.e. the optimal  $P_{SVD}$  will be lower.

#### 4.2.2 Optimal fixed truncation parameter for curves with and without the presence of recirculation

Kosior et al. [24] reported that CBF calculations are immune for tracer recirculation. However this was investigated using tracer concentration curves without noise. In practice all MRI signals contain noise, therefore it is important to investigate whether CBF calculations are immune for tracer recirculation in the presence of noise as well.

#### Method

To check if CBF calculations are independent of tracer recirculation, tracer concentration-time curves with and without recirculation are created using exponential residue function and the CBV and CBF parameters as described in subsection 4.2.1. Data is simulated over a time range of 250 seconds to avoid truncation of the curves including recirculation using the longest MTT time (24s).

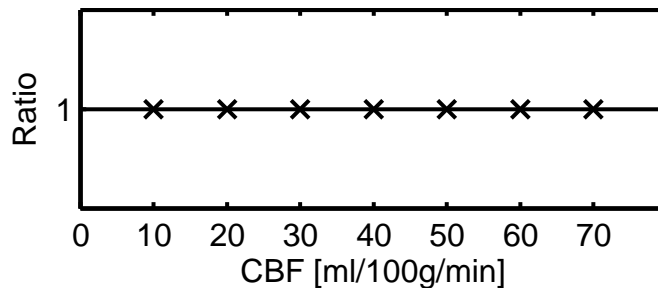
To validate the findings reported in the article [24], CBF estimates are calculated using curves without noise. Because these curves do not contain noise, weighting of the AIF matrix as described by Equation 2.12 is not

performed and  $P_{SVD}$  is set to  $5e^{-7}$  which is equal to the  $P_{SVD}$  used in the article by Kosior et al. [24].

Finally noise is added, as described in subsection 4.1.4, to obtain signals with SNR 20 and 100. Optimal  $P_{SVD}$ 's are calculated for the curves with recirculation and compared with the  $P_{SVD}$ 's of the curves without recirculation. Subsequently CBF estimates are calculated for  $CBV = 4\%$  and CBF is 10-70 mL/100 g/min with 10 mL/100 g/min increments using tSVD and block-circulant SVD with the  $P_{SVD}$ 's determined with the curves without recirculation.

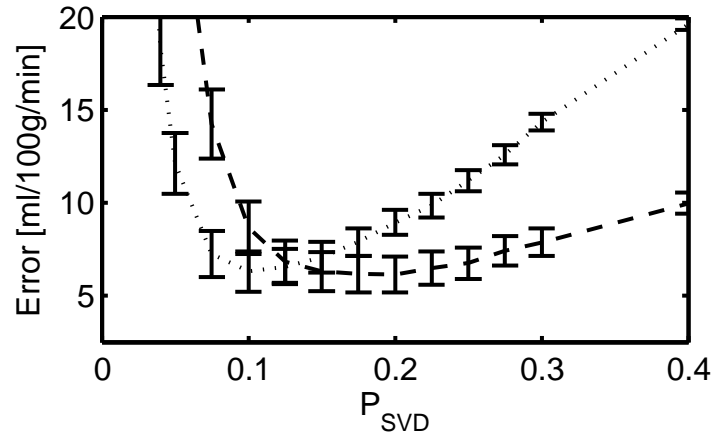
### Result

Figure 4.5 shows the  $CBF_{withrecirculation}/CBF_{withoutrecirculation}$  ratio calculated using tSVD and noise-free curves. When this ratio is one, the CBF estimates of the curves with and without recirculation is equal. This means that the CBF estimates are not influenced by tracer recirculation. So based on the figure it can be concluded that CBF estimates are not influenced by the presence of tracer recirculation when it is investigated with noise-free tracer concentration curves. The same curve is found using rSVD and block-circulant SVD.



**Figure 4.5:** *The effect of tracer recirculation. The plot shows the ratio between the CBF estimates of curves with recirculation and curves without recirculation. The line represents the ideal situation. The crossed markers indicate the CBF ratios calculated using tSVD. The graphs shows that CBF estimates are equivalent for curves with and without tracer recirculation.*

For the following results tracer concentration curves including noise with SNR 20 and 100 are used. In Figure 4.6 the error curves for determination of the optimal  $P_{SVD}$ 's are depicted. The optimal  $P_{SVD}$  for curves with recirculation is lower compared to the optimal  $P_{SVD}$  for curves without recirculation. However the mean error and standard deviation of both types of curves is comparable. The obtained  $P_{SVD}$ 's are listed in Table 4.2.



**Figure 4.6:** Mean error curve of curves with (dotted-line) and without (dashed-line) recirculation using  $tSVD$ . The depicted graph is for SNR 20. The errorbars represent 1SD.

	SNR	with recirculation	without recirculation
tSVD	20	10%	20%
	100	4%	10%
block-circulant SVD	20	7.5%	10%
	100	2%	3%

**Table 4.2:** Optimal  $P_{SVD}$  values for curves with and without recirculation using truncated SVD and block-circulant SVD. Optimal value is obtained using tissue concentration-time curves made with an exponential residue function.

Subsequently using the optimal  $P_{SVD}$  of the curves without recirculation, CBF estimates are calculated for  $CBV = 4\%$  and CBF is 10-70 mL/100 g/min with 10 mL/100 g/min increments. Figure 4.7 shows the CBF estimates calculated using tSVD and curves with SNR 100. It can be seen that the curves with recirculation are more underestimated than curves without recirculation. This was valid for both tSVD and block-circulant SVD and both SNR values.

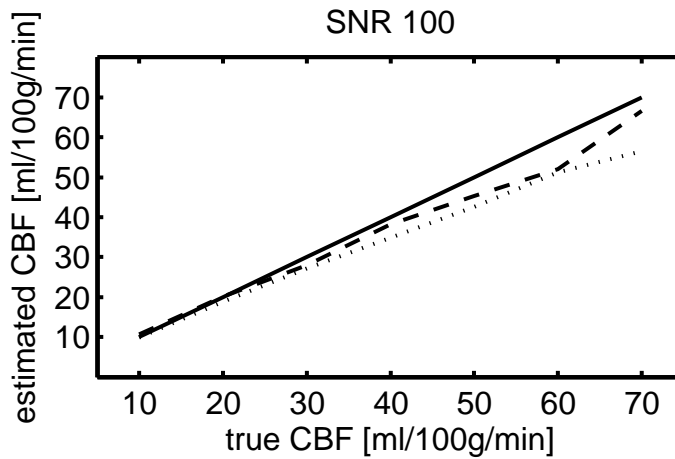


**Figure 4.7:** CBF estimation using tSVD with fixed  $P_{SVD}$  (10%) based on curves without recirculation. The figure shows  $CBV = 4\%$  with CBF is 10-70 ml/100g/min with (dotted-line) and without(dashed-line) recirculation.

## Discussion

Kosior et al. [24] have shown that tracer recirculation does not impact estimations of CBF. They investigated this with noise-free tissue concentration curves. Using noise-free curves these findings are validated (see Figure 4.5) for both tSVD and block-circulant SVD. Although CBF estimates are theoretically not influenced by the presence of tracer recirculation, Figure 4.6 shows that there is a difference in optimal  $P_{SVD}$  for curves with and without recirculation when noise is added to the curves. The error and the standard deviation of the error are equal because the curves have the same SNR.

When the optimal  $P_{SVD}$  of one type of curves is selected, the curves of the other type will be over or underestimated. For instance, when the  $P_{SVD}$  of curves without recirculation is selected, the curves with recirculation will be underestimated (see Figure 4.6). When one single image contains curves with and without recirculation, the error of the CBF estimates will differ between the voxels.

### 4.2.3 CBF estimation with different deconvolution approaches and methods to determine $P_{SVD}$

It is important to know which deconvolution approach performs best. Therefore the performance of the different approaches is compared. Furthermore the determination of the  $P_{SVD}$  is of importance, therefore methods to determine  $P_{SVD}$  are investigated as well.

#### Method

For this comparison, curves obtained with exponential residue function with  $CBV = 2\%$  with  $CBF = 5-35$  mL/100 g/min in 5 mL/100 g/min increments and  $CBV = 4\%$  with  $CBF = 10-70$  mL/100 g/min in 10 mL/100 g/min increments are used. The curves are simulated over a time range of 250 s and include recirculation. First CBF estimates are calculated using noise-free curves with tSVD, rSVD and block-circulant SVD. As described in subsection 4.2.2 the AIF matrix is not weighted and  $P_{SVD}$  is set to  $5e^{-7}$ . Subsequently noise is added to obtain curves with SNR 20 and 100.

For all 14 curves the CBF estimates are calculated using tSVD, rSVD and block-circulant SVD. All methods are performed with fixed  $P_{SVD}$ 's based on the curves with recirculation (Table 4.2) and  $P_{SVD}$ 's determined per voxel using GCV and LCC. Finally SFTR with GCV and LCC is calculated as well.

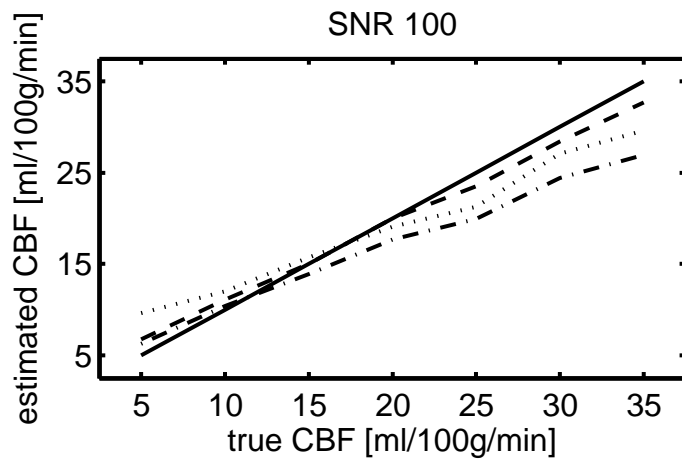
The error is calculated according to Equation 4.11 using  $N_f = 7$ .

#### Result

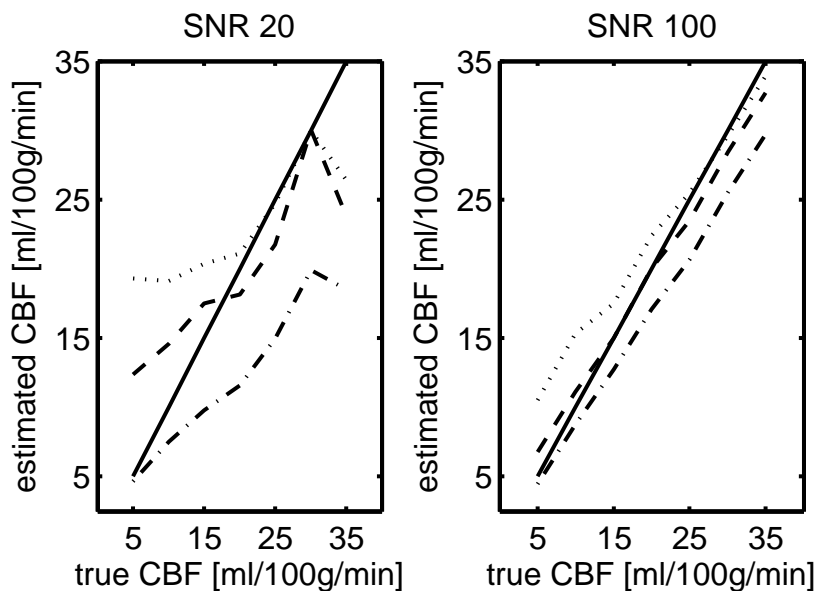
The three deconvolution approaches (tSVD, rSVD and block-circulant SVD) perform equally without the presence of noise (results not shown). All approaches are able to reproduce the true CBF. However, in the presence of noise the performance of the different approaches is not equal (Figure 4.8). When curves with SNR 100 and  $CBV = 4\%$  or  $2\%$  are used, the tSVD approach performs best followed by block-circulant and reformulated SVD respectively. Using curves with SNR 20 the differences between the approaches increases, but still the tSVD approach performs the best.

Figure 4.9 shows the CBF estimates calculated using the tSVD approach with fixed  $P_{SVD}$  and  $P_{SVD}$  determined using GCV and LCC. In both cases, SNR 20 and 100, fixed  $P_{SVD}$  provides the best CBF estimation, i.e. the lowest error, followed by LCC and GCV  $P_{SVD}$  respectively. This is found to be the same for all deconvolution approaches, CBV values and SNR values.

Finally CBF estimates are calculated using SFTR. Figure 4.10 shows that the SFTR approach with the  $P_{SVD}$  based on GCV performs best, followed by the tSVD with GCV and SFTR with LCC  $P_{SVD}$ 's respectively.



**Figure 4.8:** CBF estimates using *tSVD* (dashed-line), *rSVD* (dash-dot-line) and block-circulant SVD (dotted-line). The  $P_{SVD}$ 's are listed in Table 4.2. The solid line represents the true CBF. The figure shows  $CBV = 2\%$  with  $CBF = 5-35$  ml/100g/min including recirculation.



**Figure 4.9:** CBF estimates using fixed (dashed-line), GCV (dash-dot-line) and LCC (dotted-line) based  $P_{SVD}$ 's. The solid line represents the true CBF. The figure shows  $CBV = 2\%$  with  $CBF = 5-35$  ml/100g/min including recirculation.

These findings are the same for curves with  $CBV = 2\%$ . For curves with SNR 100 there is no difference between the performance of the approaches.

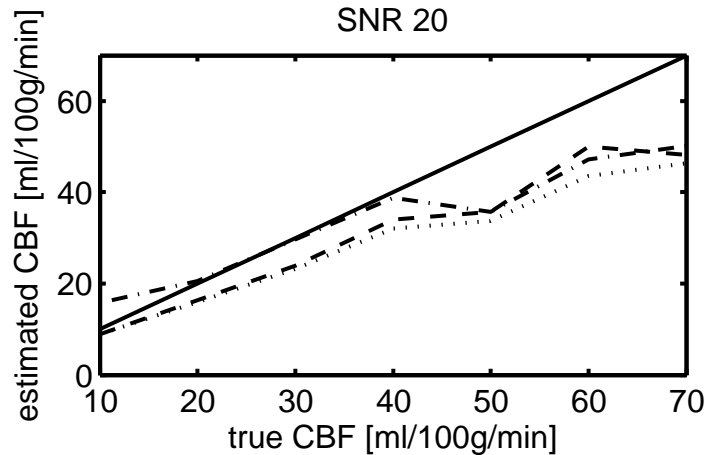


**Figure 4.10:** CBF estimates using GCV tSVD (dashed-line) and using SFTR with GCV (dash-dot-line) and LCC (dotted-line) based  $P_{SVD}$ 's. The solid line represents the true CBF. The figure shows  $CBV = 4\%$  with  $CBF = 10-70$  ml/100g/min including recirculation.

## Discussion

All methods perform equally when noise-free concentration curves are used. This is because the same underlying deconvolution technique is used. When noise is added to the concentration curves, differences between the deconvolution approaches become visible. Figure 4.8 shows that tSVD performs better compared to the other approaches. This higher underestimation using block-circulant SVD is reported by Wu et al. [19] as well. They found an underestimation of the CBF estimates when they use the block-circulant SVD approach as described in this report. However, they also provide a slightly different method to reduce the oscillations instead of the fixed  $P_{SVD}$ . Using a modified oscillation index the  $P_{SVD}$  is varied until the estimated residue function's oscillation index falls below a user-specified value. In this way the  $P_{SVD}$  is optimized per concentration time curve. Using this modified oscillation index they found better CBF estimates compared to the tSVD and standard block-circulant SVD approach as used in this report. For rSVD the  $P_{SVD}$  of the standard tSVD is used. It is possible that this  $P_{SVD}$  is too high for rSVD and causes underestimation of the CBF.

Furthermore the influence of  $P_{SVD}$ 's determined using GCV and LCC is investigated as well. The total error over the whole range of CBF values is calculated to determine the best approach. The results show that,

looking at the whole range of CBF values, in all cases the fixed tSVD approach is superior to the tSVD approach using voxel-by-voxel calculated  $P_{SVD}$ 's. Figure 4.9 shows that for SNR 20 and 100 the LCC determined  $P_{SVD}$  performs better for high CBF while the fixed  $P_{SVD}$  performs better for low CBF. In this investigation, the  $P_{SVD}$  for fixed tSVD is optimized for the tissue concentration curves which are used. However, in practice the perfusion values are unknown, and therefore the optimal  $P_{SVD}$  is unknown. So it could be expected that voxel based determination of the  $P_{SVD}$  will perform better when there is a great variety in perfusion values and residue functions. Sourbron et al. [37] suggest to use information of the neighbor voxels to minimize noisy pixels in the GCV and LCC approaches.

Besides tSVD it is possible to perform a smoother truncation using SFTR. For SFTR the  $P_{SVD}$ 's are determined using GCV and LCC. Figure 4.10 shows that the GCV approach provides the best CBF estimates. For low SNR the SFTR approach using GCV is superior to the tSVD approach while the SFTR approach using LCC is comparable to the tSVD approach. This is comparable to the findings reported by Calamante et al. [56].

#### 4.2.4 Estimating CBF in the presence of delay or dispersion

The AIF is selected in a major vessel. Therefore delay and dispersion can occur between the location of AIF measurement and the tissue. In this investigation the performance of the different deconvolution approaches is compared in the presence of delay and dispersion.

##### Method

Three tissue concentration-time curves obtained with exponential residue function are used for this comparison. The curves represent gray and white matter and hypoperfused tissue [18]. These curves include recirculation and are simulated over a time range of 250 seconds to avoid truncation of the curves with the longest MTT times. The perfusion values used for this dataset are listed in Table 4.3.

Tissue	CBV (ml/100g)	CBF (ml/100g/min)	MTT (s)
White matter	4	60	4
Gray matter	2	20	6
Hypoperfused tissue	1.8	12	9

**Table 4.3:** *CBV, CBF and MTT values of the three different tissue types.*

The optimal  $P_{SVD}$  is dependent on the CBF value [39]. Therefore the optimal  $P_{SVD}$  is calculated using the described concentration-time curves including curves with CBF - 10% and CBF + 10%. In summary, three CBF values combined with three CBV values give nine concentration-time curves involved in the optimal  $P_{SVD}$  calculation.

To evaluate the sensitivity of CBF estimates to differences in tracer arrival times between the AIF and tissue signal, the tissue curves are shifted with respect to the AIF from -4 till +6 seconds with increments of 1 second. Delays between 2-3 seconds are not uncommon in patients with cerebrovascular disease, and the 6-sec delay limit was chosen to include all delays that are observed in practice by Calamante et al. [41].

To evaluate the sensitivity to dispersion, data is simulated with values of  $1/\beta$  up to 5.5 seconds. This represents an extreme case according to Calamante et al. [41].

Firstly, CBF estimates are calculated with noise-free curves, non-weighted AIF matrix and  $P_{SVD} = 5e^{-7}$ . Secondly the CBF estimates are calculated with curves with SNR 20 and 100. The calculations are done using tSVD, rSVD and block circulant SVD. All methods are performed with fixed  $P_{SVD}$ 's based on the curves with recirculation (Table 4.2) and  $P_{SVD}$ 's determined using GCV and LCC. Finally SFTR with GCV and LCC is calculated as well.

## Result

First the optimal  $P_{SVD}$ 's are determined based on the tissue concentration-time curves which are described in the methods. The optimal  $P_{SVD}$ 's for SNR 20 and 100, tSVD and block-circulant SVD are listed in Table 4.4. These values are used during the following steps of this investigation.

SNR	tSVD	block-circulant SVD
20	10%	7.5%
100	5%	2%

**Table 4.4:** Optimal  $P_{SVD}$  values using tSVD and block-circulant SVD. The optimal value is obtained using tissue concentration-time curves made exponential residue functions and the perfusion values listed in Table 4.3.

This investigation can be divided into two parts, namely CBF estimates calculated in the presence of delay and CBF estimates in the presence of dispersion. First the results related to delay are described.

Figure 4.11 shows the  $CBF_{estimated}/CBF_{true}$  ratio for noise-free curves calculated using tSVD and block-circulant SVD. rSVD shows exactly the same results as block-circulant SVD, for clarity only block-circulant SVD is

shown. CBF estimates calculated with the tSVD approach are overestimated in the presence of negative delays and well estimated with delays greater than zero. Furthermore the figure shows that CBF estimates calculated with block-circulant SVD are delay independent within this range of delays.

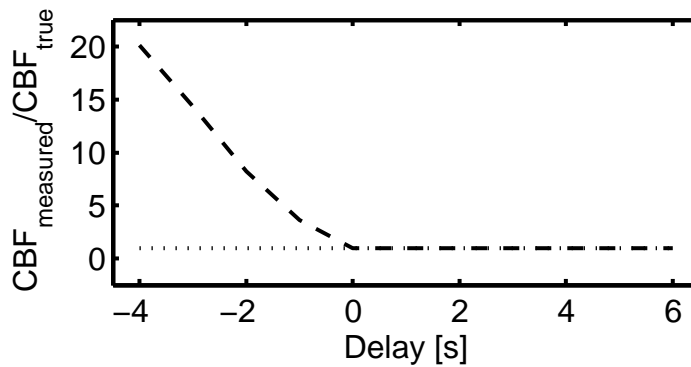


**Figure 4.11:** The effect of delay on CBF estimates of hypoperfused tissue curves. The plot shows the ratio between the CBF estimates and the true CBF. The graph includes tSVD (dashed-line) and block-circulant SVD (dotted-line).

In the presence of noise the same patterns can be recognized. Figure 4.12 shows that regardless of the CBV and CBF values tSVD overestimates CBF for negative delays and performs equal to block-circulant and rSVD for delays greater than zero. SFTR shows the same delay dependent results as tSVD.

The solid lines in Figure 4.13 show for noise-free concentration curves the  $CBF_{estimated}/CBF_{estimatedwithoutdispersion}$  ratio. All deconvolution approaches perform equal, therefore only one line is visible. The figure shows that all approaches are dependent on the amount of dispersion. When noise is added to the curves dependency on CBF is seen as well. The figure shows that the delay independent approaches provide a higher  $CBF_{estimated}/CBF_{estimatedwithoutdispersion}$  ratio. Furthermore the SFTR approach performs equal to the block-circulant and rSVD approaches (results not shown).

## Discussion

The optimal  $P_{SVD}$ 's of the tissue concentration curves, representing the three types of tissues, are comparable to the  $P_{SVD}$ 's of the curves with recirculation reported in subsection 4.2.2.

The  $CBF_{estimated}/CBF_{true}$  ratio gives the information that the CBF

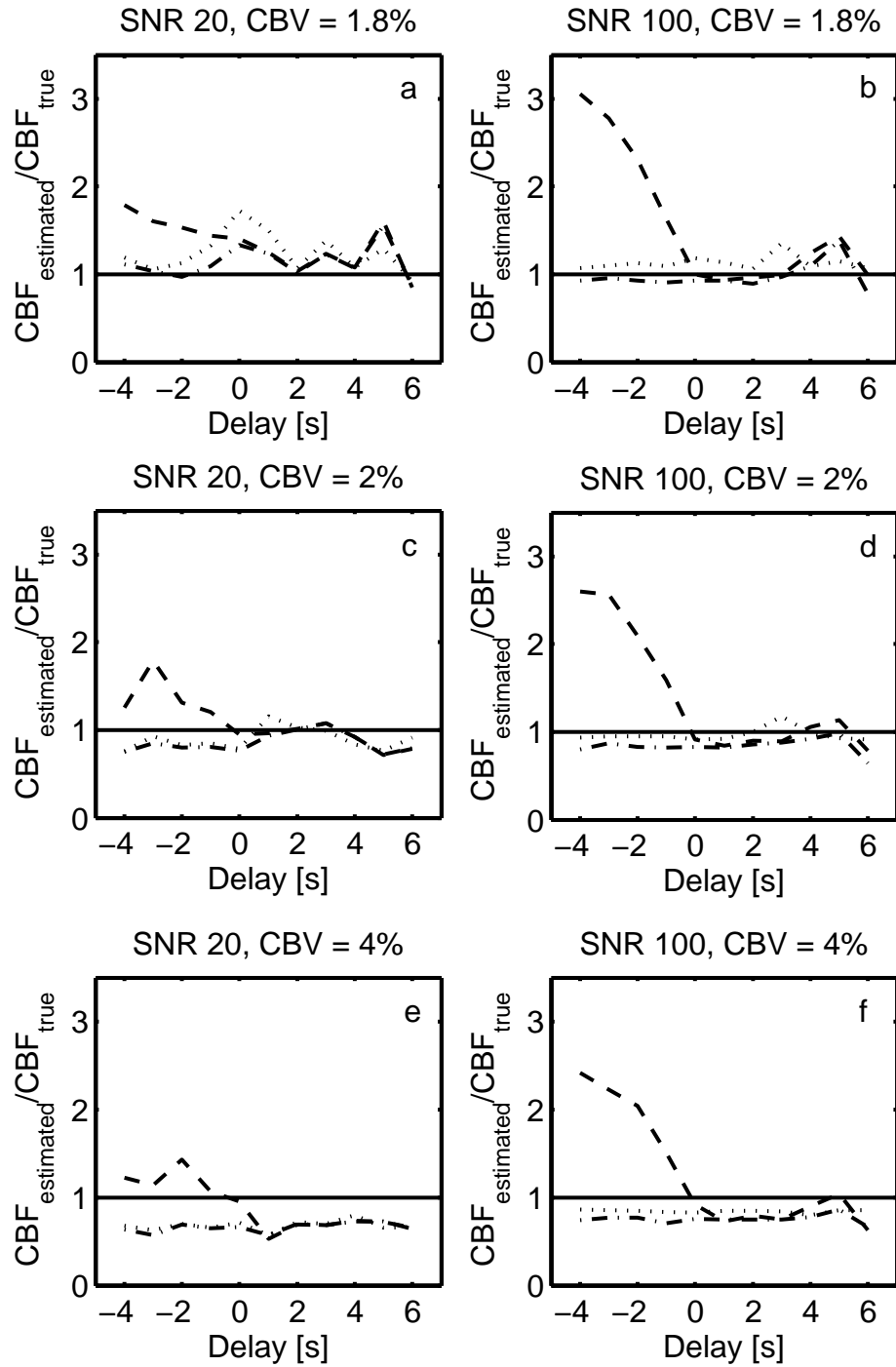


**Figure 4.12:** The effect of delay on CBF estimates. The plots show the ratio between the CBF estimates and the true CBF. a,c,e) SNR 20 with CBV = 1.8 2 and 4% respectively. b,d,f) SNR100 with CBV = 1.8 2 and 4% respectively, for tSVD (dashed-line), rSVD (dash-dot-line) and block-circulant SVD (dotted-line). The solid line shows the ideal ratio.

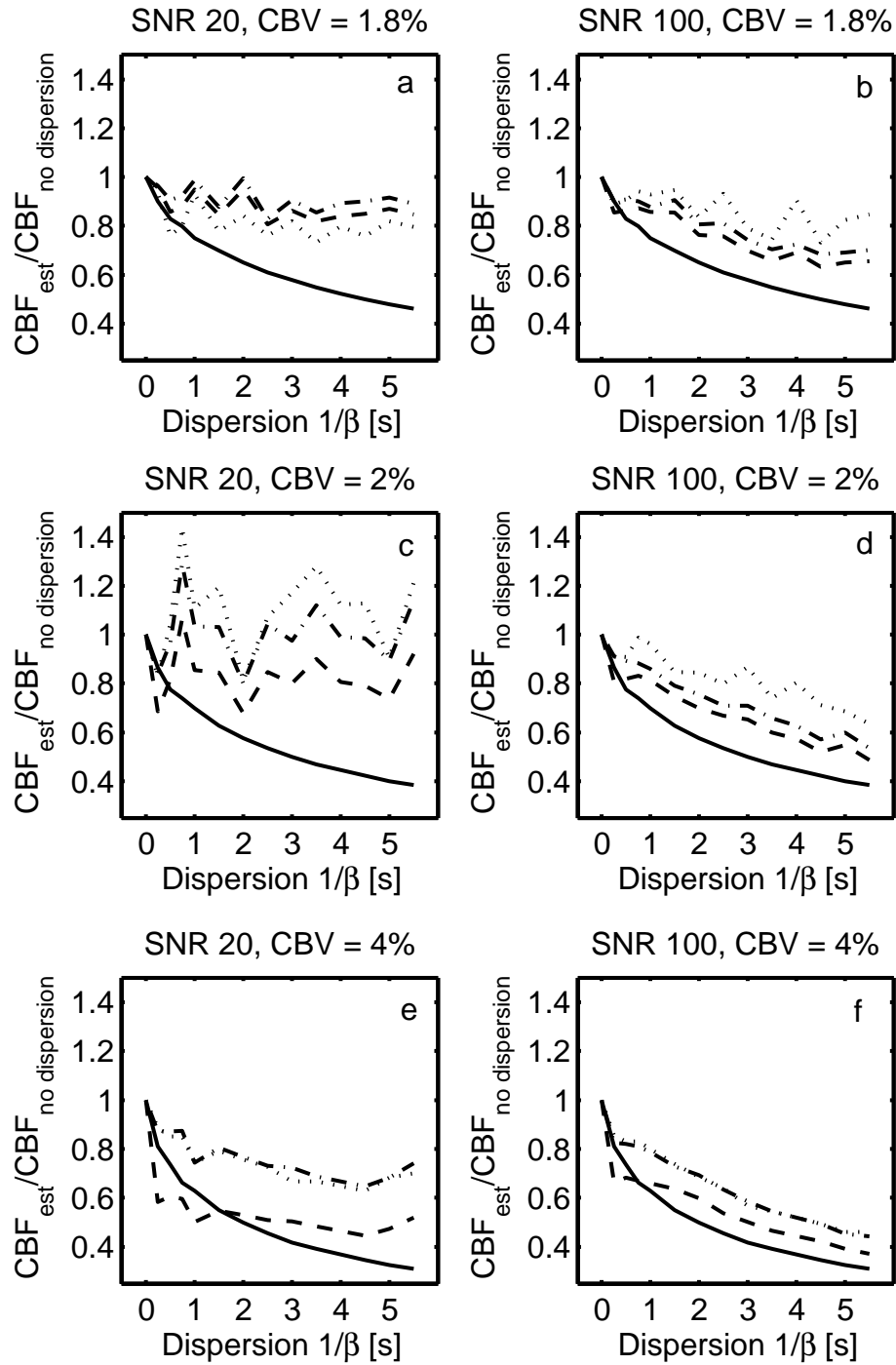


**Figure 4.13:** The effect of dispersion on CBF estimates. The plots show the ratio between the CBF estimates and CBF estimate of a curve without dispersion. a,c,e) SNR 20 with CBV = 1.8 2 and 4% respectively. b,d,f) SNR100 with CBV = 1.8 2 and 4% respectively. The solid line shows the CBF estimates calculated with noise-free curves. tSVD (dashed-line), rSVD (dash-dot-line) and block-circulant SVD (dotted-line) are the approaches used.

estimate calculated with the tSVD approach is dependent of the delay. In the presence of negative delays, i.e. the peak of the tissue concentration curve will appear before the peak in the AIF, the tSVD approach will overestimate the CBF values. For delays equal to or larger than zero seconds tSVD becomes delay independent. Block-circulant and rSVD approaches are delay independent for negative delays as well. Also when noise is added to the curves, block-circulant and rSVD are able to estimate CBF near the true CBF for negative delays. With noise the tSVD approach is delay independent for delays larger than one second. Without noise and a delay of -4 seconds, the tSVD approach gives an estimated CBF which is 20 times the true CBF. The curves with noise do not show such a large overestimation due to the truncation of the eigenvalues.

The block-circulant and rSVD approaches seem to be delay independent. However, the delay is varied from -4 till 6 seconds with increments of 1 second, which is equal to the TR of the signal. Salluzzi et al. [57] reported that the  $CBF_{measured}/CBF_{true}$  changes with a period equal to TR. This variation is unwanted. When different voxels have different delays, the error of the CBF estimates will differ between the voxels as well. So further investigation to the delay independency of block-circulant and rSVD is necessary.

Using SFTR the CBF estimates are delay dependent as well. This could be expected because the SFTR approach is equal to the tSVD approach, only the truncation is smoother. Therefore the delay dependent behavior of the tSVD approach is still present using the SFTR approach.

When dispersion is added to the noise-free tissue concentration curves, all approaches are unable to reproduce the true CBF. This is reported in several other articles as well [41, 58, 59]. The performance of all approaches using noise-free curves is equal. However, when noise was added to the curves, the delay independent approaches perform better. Ko et al. [58] reported a difference between the approaches as well.

Adding dispersion to the tissue concentration curves causes broadening of the bolus and subsequently a shift of the peak. According to Ko et al. [58] this is the reason why tSVD underestimates the CBF more in the presence of bolus dispersion. This is found in our investigation as well. Namely with zero seconds delay, the tSVD approach gives a higher CBF estimation compared to one second delay (see Figure 4.12). Therefore the CBF estimate without dispersion and therefore zero delay is higher for tSVD compared to block-circulant and rSVD. For a dispersion constant  $1/\beta = 0.25$  seconds a delay of one second exists which causes a change in CBF estimate due to both the bolus broadening and the additional delay. After one second delay, comparable to  $1/\beta = 0.25$  s, the  $CBF_{estimate}/CBF_{true}$  ratio becomes constant and the CBF estimates are only dependent on the amount of dispersion. Therefore the shape of the curves become equal after  $1/\beta = 0.25$  s.

Furthermore Murase et al. [39] investigated the relationship between the optimal  $P_{SVD}$  and the amount of dispersion. Figure 8 in their report shows that for dispersion constants below 5 seconds the optimal  $P_{SVD}$  changes. The larger the amount of dispersion, the lower the optimal  $P_{SVD}$ . When a lower  $P_{SVD}$  is selected, a higher CBF estimation will be provided. It could be possible that block-circulant and rSVD approaches have a different dependency on the  $P_{SVD}$  or are less dependent on the  $P_{SVD}$  because without dispersion the  $P_{SVD}$  is already lower.

Finally the performance of the SFTR approach is comparable to the block-circulant and rSVD approaches. This is comparable to the findings by Calamante et al. [56]. They reported that the SFTR approach provides a more accurate representation of the initial part of the residue function in the presence of dispersion.

#### 4.2.5 Estimating CBV

As described in section 2.4 CBV can be calculated using several methods. This investigation is performed to check if there is a difference in the ability to provide the true CBV between the integration methods.

##### Method

For this investigation, the tissue concentration-time curves as described in subsection 4.2.3 are used. CBV is calculated using Equation 2.4. Therefore the area beneath the tissue concentration curves and the AIF are needed. To calculate the CBV, there are different integration methods which can be used. The same integration method is used for both the tissue concentration curves and the AIF. Four methods are compared using the simulated curves:

1. **Whole area:** *Integration over the whole time cycle.*

For this method, the discrete  $C_t(t)$  data is used directly. The integration boundaries are the arrival time of the tracer contrast bolus and the end of the acquisition time. To determine the arrival time of the bolus, the mean signal intensity-time curve over all voxels and its standard deviation is calculated. Then the arrival time is determined as the time when the signal intensity exceeds five times the standard deviation.

2. **First pass:** *Integration over the first pass.*

The start of the integration boundaries is equal to the first boundary of the whole time cycle method, namely the arrival time of the tracer contrast bolus. The end of the integration boundary is reached when the mean tissue concentration curve, calculated over all voxels, drops below 30% of the peak concentration.

3. **Gamma variate:** *Integration with gamma variate fit.*

For this method, first a gamma variate function is fitted to the AIF and tissue concentration curves. The fitting of the gamma variate function is described in Appendix A. Before the fitting procedure, the AIF and tissue concentration curves are smoothed equivalently to Equation 2.12. Finally the area under the fitted curves is calculated.

4. **Deconvolution area:** *Integration of the area under the tissue impulse response function.*

During the CBF calculation, the tissue impulse response function is estimated using deconvolution. The area under the function is equal to the CBV as well. In this method, the area under the AIF is not needed. During this investigation tSVD using optimal fixed  $P_{SVD}$  as determined in subsection 4.2.1 is used.

For both CBV values, fourteen CBV estimates are obtained, namely for seven CBF values combined with two SNR values. To compare the performance the mean CBV estimate over the seven CBF values is calculated. In summary, for every CBV value and SNR one mean CBV estimate is obtained.

## Result

Four types of integration are used during this investigation. For every CBV (2% and 4%) seven CBF values are used. The mean of the estimated CBV over these seven CBF values is calculated and listed together with the standard deviation in Table 4.5. The gamma variate fitting method has some outliers because the algorithm was not always able to fit the curve. These outliers are removed before calculation of the mean CBV.

CBV SNR	4%		2%	
	20	100	20	100
whole area	$4.31 \pm 1.73$	$4.32 \pm 0.29$	$2.52 \pm 1.51$	$2.21 \pm 0.26$
first pass	$2.52 \pm 17.6$	$3.94 \pm 0.24$	$2.59 \pm 27.1$	$1.98 \pm 0.12$
gamma variate	$6.46 \pm 2.80$	$7.14 \pm 2.35$	$3.13 \pm 4.42$	$3.59 \pm 1.10$
deconvolution	$3.94 \pm 1.86$	$4.01 \pm 0.28$	$2.29 \pm 1.46$	$2.05 \pm 0.27$

**Table 4.5:** *The CBV estimates using four integration methods. The CBV estimates are the mean over seven CBF values. For the gamma-variate method, the outliers are first removed.*

The table shows that the whole area and deconvolution area integration methods both perform better than the first pass and gamma variate methods. Furthermore using curves with SNR 100 a better estimate is provided.

## Discussion

For this investigation, four different integration methods are implemented. The gamma variate fitting procedure as currently implemented was not a robust algorithm. The algorithm was able to fit the first pass of the AIF for all SNR and CBF values. However for the tissue concentration curves, the algorithm was not able to distinguish the first pass from the recirculation. Therefore the gamma variate fit of the tissue concentration curves includes the recirculation as well and the CBV is overestimated.

The three other methods only use the discrete concentration data. The whole area method overestimates the CBV but with a relative small standard deviation. This small standard deviation is caused by the amount of samples used in the integration. The first pass method underestimates the CBV with a factor 1.5 and has for SNR 20 a high standard deviation. In contrary to the whole cycle method, just 5 to 9 samples are used in this integration. This small amount of samples causes the large standard deviation. Furthermore during this investigation simulated datasets containing only one type of concentration curves, i.e. based on one CBF and one CBV value, are used at once. This means that the mean curve over all voxels is based on just one set of values. In practice multiple perfusion values are present in one image. The integration boundaries are determined using the mean curve over all voxels. So it can be expected that curves with long MTTs will be underestimated while curves with short MTTs will be overestimated.

Finally the area under the tissue impulse response function gives a good CBV estimate with a low standard deviation.

When the mean CBV is over or underestimated, but with a small standard deviation, the error between the voxels in the image will be constant. When the mean CBV is estimated well, but with a large standard deviation, the error between the voxels in the image will be different. It is preferred to have a method which gives a good CBV estimate with a low standard deviation. Therefore the area below the deconvolution area is preferable. This is found by Perkiö et al. [18] as well. They reported that integration over the whole cycle is preferable for relative CBV measurements while the area under the deconvolved curve provides the most accurate estimates for absolute CBV.



---

## Clinical data

*After comparison of different post processing methods with simulated data, the methods can be compared using clinical data as well. This chapter gives a short comparison between the different methods using clinical data obtained from 15 patients with a transient ischemic attack (TIA). First the MRI acquisition is mentioned in section 5.1. Subsequently the comparison which is done is explained in section 5.2. This section consists of a method, result and discussion part.*

### 5.1 Clinical data MRI acquisition

The analysis of the clinical data is performed retrospective. All data is obtained between may 2006 and may 2008. The data of 15 patients, 10 female and 5 male, (age:  $55.7 \pm 11.4$  (mean  $\pm$  SD)) suffering from a TIA is used. Contrast-enhanced T2\* weighted images were collected using a gradient-echo sequence (TR/TE = 2280ms / 47ms ) on a clinical MR scanner (Siemens). During the imaging sequence, contrast agent (Dotarem) was injected. All studies consisted of 19 slices with a thickness of 5mm collected over 30 timepoints.

### 5.2 Comparison

When clinical data is used, the true perfusion values are unknown. Therefore the methods are compared to each other to get an idea of the differences between the methods. A graphical user interface is made to investigate the datasets. An overview of the graphical user interface is given in Appendix B. It is possible to run the quantifications as scripts as well.

## Method

From the clinical MR data, first the skull is removed from the dataset by thresholding of the image. Subsequently concentration time curves have to be calculated for every voxel. This is done using Equation 2.2. To determine the CBF and CBV the AIF has to be known. In this investigation an automatic AIF-identification algorithm is used as described by Carroll et al. [26]. All data are quantified by tSVD, rSVD and block-circulant approaches with the  $P_{SVD}$ 's as determined in subsection 4.2.1 for SNR 20. This SNR is comparable to the SNR of clinical data [19, 56]. The CBV is calculated by integration of the area under the tissue impulse response function.

After calculation of the CBF maps, the percentage difference between the methods is calculated. This is the absolute difference between the two methods divided by the average value of the two methods. This can be written in equation form:

$$\%Difference = \frac{M_1 - M_2}{(M_1 + M_2)/2} \cdot 100, \quad (5.1)$$

where  $M_1$  and  $M_2$  are the CBF values of method 1 and method 2 respectively. Finally the mean percentage difference and its standard deviation over all voxels in the dataset is calculated.

## Result

Table 5.1 shows the mean percentage difference between the methods calculated using all voxels in the dataset. A positive percentage difference indicates that the first method has higher CBF values than the second method. So the tSVD approach provides higher CBF estimates compared to rSVD.

Figure 5.1 shows one example of a percentage difference image for one brainslice. The figure shows that the percentage difference is not equal for the whole brain slice. For example in the figure, the percentage difference in white matter is negative, while the percentage difference in gray matter is positive. This is shown by the large standard deviations in Table 5.1 as well.

## Discussion

The comparison using clinical data is just performed to give an indication between the differences of the methods. The percentage difference is calculated over the whole acquired dataset. In some datasets, voxels of the skull are still included in the calculations because they had the same signal intensity as brain voxels. The percentage differences differ between brain slices,

Patient nr.	% Difference		
	tSVD vs. rSVD	tSVD vs. bcSVD	rSVD vs. bcSVD
1	43.5 ± 23.2	-2.89 ± 15.7	-46.3 ± 22.4
2	37.8 ± 21.8	-7.92 ± 12.8	-45.4 ± 21.2
3	23.9 ± 33.1	-28.3 ± 19.9	-51.4 ± 26.0
4	41.5 ± 35.3	-12.8 ± 15.7	-52.9 ± 36.4
5	43.3 ± 27.5	-9.39 ± 14.2	-52.1 ± 26.2
6	26.1 ± 33.5	1.17 ± 19.5	-25.1 ± 32.5
7	32.8 ± 25.6	-3.45 ± 12.1	-36.3 ± 15.6
8	-0.98 ± 21.3	-12.0 ± 16.3	-10.9 ± 17.0
9	59.6 ± 35.3	-3.87 ± 21.2	-63.0 ± 34.5
10	15.9 ± 23.9	-8.38 ± 18.1	-24.0 ± 26.5
11	13.4 ± 23.1	-4.98 ± 12.2	-18.2 ± 22.6
12	18.6 ± 23.4	-7.15 ± 16.7	-25.6 ± 24.2
13	22.8 ± 29.6	-4.09 ± 10.9	-26.7 ± 30.1
14	14.5 ± 18.9	6.82 ± 16.0	-7.78 ± 22.2
15	10.3 ± 26.5	-11.6 ± 19.1	-21.4 ± 28.6
mean ± SD	26.9 ± 26.8	-7.25 ± 16.0	-33.8 ± 25.7

**Table 5.1:** Percentage difference between *tSVD*, *rSVD* and block-circulant *SVD* using clinical data of 15 patients.

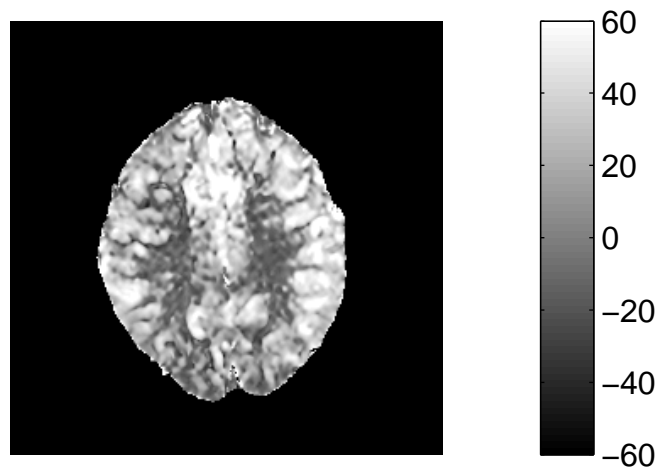


**Figure 5.1:** Percentage difference between *tSVD* and *rSVD*. A negative percentage means that *tSVD* provides a higher CBF estimate than *rSVD*. The figure shows that the percentage difference is not equal for all voxels in the brainslice. This is brain slice 13 of patient 6.

and between tissue types as can be seen in Table 5.1. The large standard deviation shows that the percentage difference is not equal for all voxels, i.e. there is a large variability of the results.

To investigate the difference between the tissue regions, ROIs should be drawn in the image and compared with each other. Then information about the CBF estimates between the different methods is obtained.

None of the datasets show regions of low perfusion. This could be expected, because the datasets are from patients with a TIA instead of a stroke.

---

# Conclusions and Recommendations

*The goal of this research project was to compare different quantification methods to select the best method for evaluation of follow-up studies. For this purpose Monte-Carlo simulations are performed to obtain data with known perfusion values. With these simulated datasets several research questions are investigated. The final selection of the best method is still not possible, therefore more research is necessary. In this chapter the research questions as described in chapter 3 are answered. Furthermore recommendations are given for further research to find the best post processing method to calculate perfusion values.*

## 6.1 Research questions

Using the simulated data the research questions as described in chapter 3 are investigated. In this section all research question will be answered.

- *Which  $P_{SVD}$  values are optimal using tSVD and block-circulant SVD with SNR 100 and 20?*

The  $P_{SVD}$  is used to truncate the eigenvalues of the AIF matrix. Due to the truncation, noise is suppressed and a more accurate CBF estimate is obtained. For SNR 20 optimal  $P_{SVD}$ 's of 22.5 and 15% for tSVD and block-circulant SVD respectively are found. For SNR 100 these values were 10 and 4% respectively. These values are comparable to the values reported by other researchers [19, 20].

- *Is CBF immune to tracer recirculation in the presence of noise as well?*

Kosior et al. [24] reported that CBF estimates are immune for tracer recirculation. This is indeed valid for noise-free tissue concentration

curves. However, when noise is added to the curves the optimal  $P_{SVD}$  is different between the curves with and without recirculation. For example using tSVD, an optimal  $P_{SVD}$  of 20% is found for curves with SNR 20 without recirculation, and an optimal  $P_{SVD}$  of 10% is found for these curves with recirculation. The differences in optimal  $P_{SVD}$  cause differences in the error of the CBF estimates between voxels within one image. This differences in errors can cause misinterpretations which can have influences on clinical decisions and interpretations of follow up studies.

- *Which deconvolution method, tSVD, rSVD or block-circulant SVD, provides the best CBF estimations? And which method to determine  $P_{SVD}$  performs best?*

All deconvolution approaches were applied to different concentration time curves to investigate the differences between the approaches. With these curves and the optimal  $P_{SVD}$ 's which are optimized for the curves used, tSVD is found as the best method. Furthermore the different regularization methods are compared. When the fixed  $P_{SVD}$  is optimized, this performs better than voxel based GCV and LCC. However, in clinical data the  $P_{SVD}$  can not be optimized. It can be expected that GCV and LCC will perform better in the presence of multiple residue types, and a width range of perfusion values.

- *Which deconvolution method, tSVD, rSVD or block-circulant SVD, provides the best CBF estimations in the presence of delay? And which method in the presence of dispersion?*

In the presence of negative delays, tSVD fails to reproduce the true CBF. Using one global AIF, negative delays are not uncommon. Therefore tSVD is not the preferred method. The SFTR approach is delay dependent as well, because only the way of truncation differs from the tSVD approach. Therefore the SFTR approach is not preferred as well. The block-circulant and rSVD approaches are both delay independent and are therefore better methods in the presence of delay.

In the presence of dispersion all methods perform comparably. However because of the delay dependency of the tSVD approach, this approach has a larger underestimation of the dispersed CBF. The SFTR approach performs better than tSVD due to the smooth truncation.

- *Which of the four CBV calculation method provides the best CBV estimations?*

CBV can be calculated in several ways. In this investigation four calculation methods are compared. The methods used in this investigation are: integration of the whole acquisition data, integration of the first pass, integration under the gamma variate fit and integration under

the tissue impulse response function obtained during deconvolution. For both SNR, 20 and 100, and both CBV values the area under the deconvolved residue function gives the most accurate CBV estimates. This is found by Perkiö [18] as well.

## 6.2 Which method is the best?

Using these research questions and the corresponding answers it is still not possible to select the best post processing approach. The estimates provided by the approaches are dependent on several factors. One important factor is the truncation parameter  $P_{SVD}$ . The optimal  $P_{SVD}$  is dependent on multiple factors such as noise, CBF and dispersion.

In this study delay and dispersion are investigated. During the investigations in this report a constant  $P_{SVD}$  is assumed for the dispersed curves. Furthermore, only a fixed dispersion, corresponding to narrowing of a vessel is investigated. Dispersion can be caused by a long vessel pathway as well, giving a dispersion constant which is dependent on the arrival time [58]. However all SVD approaches are dependent of dispersion.

Furthermore there are a lot of assumptions made during the calculations, such as the linear relationship of the concentration and the change in relaxation rate. Finally the CBF estimates are still dependent on the acquired data parameters such as the repetition time, the echo time, and so on. To compare follow up studies, it is necessary to know more about the parameters used in the calculations.

However, it is possible to say which method has the highest potential to be the best method. The tSVD and SFTR approaches are not preferable because of the delay dependent behavior of the approaches. The tSVD approach was not the best method in the presence of dispersion as well. The block-circulant and rSVD approaches are comparable. However with the block-circulant approach the tissue curves are zero padded to make the curves twice as long. This longer curves causes bigger matrices and therefore the computation time is much longer. For example with a dataset with the sizes 256 pixels x 256 pixels x 19 slices x 30 timesteps, the rSVD approach takes 200 seconds while the block-circulant approaches takes 450 seconds. However, for the rSVD approach the amount of zero padding is a manual input. The block-circulant approach works with all delay values without manual input. This is an advantage of the block-circulant method. Therefore block-circulant SVD has the highest potential.

For the CBV calculations the area under the tissue impulse response function is the most promising method. When the deconvolution is further improved, the CBV estimation is further improved as well.

### 6.3 Recommendations

As already described, the selection of the best method is still a difficult question. Therefore some recommendations are made for further research. With these recommendations more insight in the behavior of the SVD approaches is obtained. Using this additional information, hopefully the best SVD approach can be selected to compare follow up studies.

In this study it has been shown that the optimal  $P_{SVD}$  changes between curves with and without recirculation. Therefore it could be expected that voxel based determination of the  $P_{SVD}$  using GCV or LCC works better than the use of a fixed  $P_{SVD}$  when both types of curves are present. It is recommended to compare the error of CBF estimates using GCV and LCC to see if these voxel based determination of the  $P_{SVD}$  works better.

To investigate the influence of the CBF estimates in the presence of delay, only delay values which are a multiple of TR are used. Salluzzi et al. [57] reported that the  $CBF_{measured}/CBF_{true}$  changes with a period equal to TR. This variation changes with the selection of the  $P_{SVD}$ . Therefore it is recommended to investigate and compare the behavior of the approaches in the presence of delays which are not a multiple of TR.

During dispersion, broadening of the bolus occur combined with a shift of the peak concentration. Now one dispersion model is used with fixed dispersion constant. Ko et al. [58] reported that the dispersion could be delay dependent as well when the dispersion is caused by a long vessel instead of narrowing of the vessel. Furthermore, during this investigation only the CBF estimates were taken into account. However the reproduction of the shape of the residue function is of importance as well. The total shape of the residue function can be used for flow heterogeneity [56].

Unfortunately all SVD approaches are dependent on the amount of dispersion. Using a local AIF, the distance between the AIF measurement and the tissue is shortened. This shorter distance will cause less dispersion and delay and therefore more accurate CBF estimates will be obtained.

Finally during this investigation only simulated data is used. The assumptions based on the linearity of the concentration and the change in relaxation rate is not taken into account in this way. Therefore it is recommended to make a perfusion phantom and to perform real perfusion measurements using a MR machine with known perfusion values. One method to make a phantom is reported by Ebrahimi et al. [60, 61].

# A

---

## Simplified formulation of gamma variate function

The simplified formulation of the gamma variate function proposed by Madsen [54] begins with the usual form described by

$$y(t) = A \cdot (t - t_0)^\alpha \cdot e^{-(t-t_0)/\beta}, \quad (\text{A.1})$$

where  $t_0$  denotes the bolus arrival time and  $A$ ,  $\alpha$  and  $\beta$  are free shape parameters. Because  $t_0$  can be estimated easily, the origin of the graph can be shifted in such a way that it coincides with  $t_0$ . The function can then be expressed as

$$y(t) = A \cdot t^\alpha \cdot e^{-t/\beta}. \quad (\text{A.2})$$

The parameter  $\beta$  can be written in terms of  $\alpha$  and  $t_{max}$ .  $t_{max}$  is the time  $t$  at which  $y(t)$  reaches its maximum. Taking the first derivative of A.2 and setting it to zero will yield  $t_{max}$  in terms of  $\alpha$  and  $\beta$ , or  $\beta$  in terms of  $t_{max}$  and  $\alpha$ .

$$\begin{aligned} y'(t) &= 0 \\ &= A \cdot \left[ \alpha \cdot t_{max}^{\alpha-1} \cdot e^{-t_{max}/\beta} - t_{max}^\alpha \cdot e^{-t_{max}/\beta} / \beta \right] \\ &= A \cdot t_{max}^{\alpha-1} \cdot e^{-t_{max}/\beta} [\alpha - t_{max}/\beta] \end{aligned} \quad (\text{A.3})$$

$$t_{max} = \alpha \cdot \beta \text{ and } \beta = \frac{t_{max}}{\alpha} \quad (\text{A.4})$$

Substitution of  $\beta$  in Equation A.2 gives

$$y_{max} = A \cdot t^\alpha \cdot e^{-\alpha t/t_{max}} \quad (\text{A.5})$$

Subsequently letting  $t = t_{max}$  will yield  $A$  in terms of  $y_{max}$ ,  $t_{max}$  and  $\alpha$ :

$$y_{max} = y(t_{max}) = A \cdot t_{max}^{\alpha} \cdot e^{-\alpha t_{max}/t_{max}} \rightarrow A = y_{max} \cdot t_{max}^{-\alpha} \cdot e^{\alpha}. \quad (\text{A.6})$$

Substitution of  $A$  into Equation A.5 yields

$$y(t) = y_{max} \cdot t_{max}^{-\alpha} \cdot e^{\alpha} \cdot t^{\alpha} \cdot e^{-\alpha t/t_{max}} \quad (\text{A.7})$$

Using  $t' = t/t_{max}$ , Equation A.7 can be further simplified.

$$\begin{aligned} y(t') &= y_{max} \cdot t_{max}^{-\alpha} \cdot e^{\alpha} \cdot t_{max}^{\alpha} \cdot t'^{\alpha} \cdot e^{-\alpha t'} \\ &= y_{max} \cdot t'^{\alpha} \cdot e^{\alpha(1-t')} \end{aligned} \quad (\text{A.8})$$

From this equation  $y_{max}$  and  $\alpha$  can be found from a linear least-squares estimation. Taking into account that  $\ln(t^{\alpha}) = \alpha \cdot \ln(t)$ , the following equation is obtained if the natural logarithm is taken:

$$\ln(y(t')) = \ln(y_{max}) + \alpha(1 - t' + \ln(t')). \quad (\text{A.9})$$

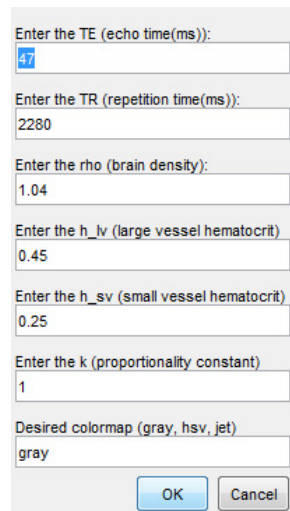
From this equation  $y_{max}$  and  $\alpha$  can be obtained. Subsequently using Equation A.4 and Equation A.6  $\beta$  and  $A$  can be calculated respectively. Finally using Equation A.1 the shape of the gamma variate fit is obtained.

# B

---

## Graphical User Interface

To investigate the differences between post processing methods a graphical user interface (GUI) is made. When the GUI is opened, first the location of the dataset on the computer is asked. Subsequently all parameters can be changed manually (see Figure B.1). With these parameters the concentration maps are calculated.



The image shows a screenshot of a graphical user interface (GUI) window. It contains several input fields for parameters, each with a label and a text box. The parameters and their values are: TE (echo time) in ms: 47; TR (repetition time) in ms: 2280; rho (brain density): 1.04; h\_lv (large vessel hematocrit): 0.45; h\_sv (small vessel hematocrit): 0.25; k (proportionality constant): 1; and Desired colormap (gray, hsv, jet): gray. At the bottom of the window are two buttons: 'OK' and 'Cancel'.

**Figure B.1:** *In this window all parameters used to calculate the concentration can be changed.*

Using the dataset panel at the right top, the total dataset can be visualized (see Figure B.2). The graph at the right bottom can show the manual selected AIF and the automatic calculated AIF using the adaptive thresholding method as described by Carroll et al. [26]. Finally when a brain voxel is selected, the concentration time curve of the selected voxel, together with

its corresponding gamma variate fit, can be shown as well.

The options panel gives the user the opportunity to select the desired deconvolution method to determine CBF, the integration method to determine CBV and the truncation method to suppress noise. Furthermore it is possible to change the method of AIF selection between manual selection by drawing a region of interest or selecting a voxel and automatic AIF selection. Finally the use of smoothed AIF and tissue data can be selected in this option panel.

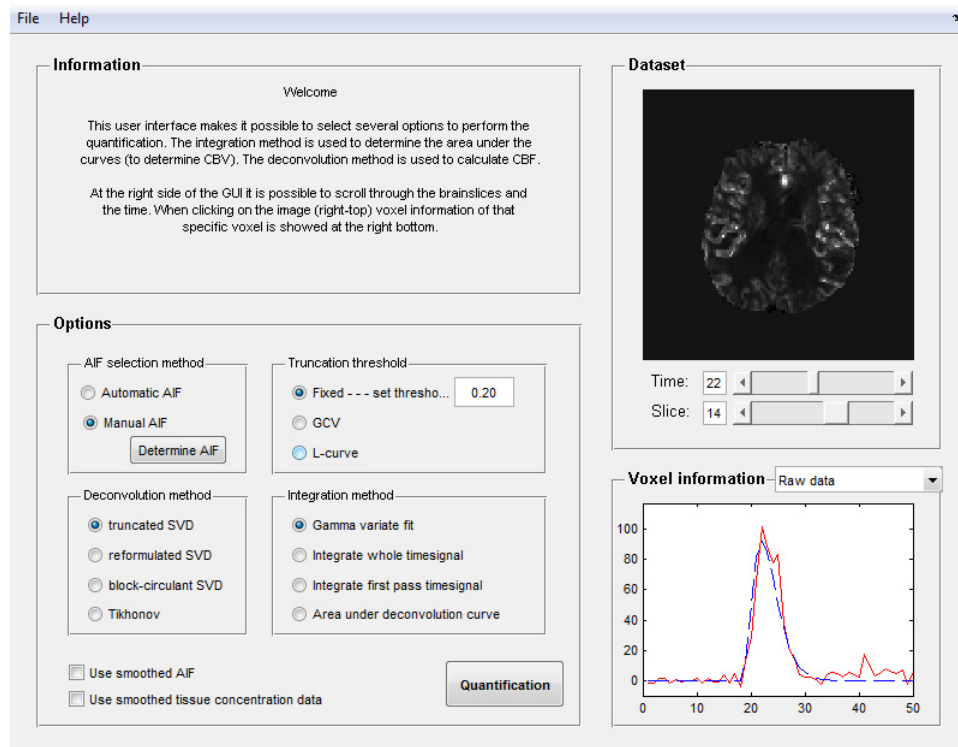


**Figure B.2:** This is the GUI which makes it possible to scroll through the dataset, select the desired quantification methods and runs the quantification.

After running the selected quantification a final window (see Figure B.3) is opened which shows the calculated CBV, CBF, MTT and TTP maps. Within this window a region of interest can be selected to calculate the mean values within this region. This final window makes it possible to scroll through the final datasets to see if there is a region of low perfusion.

Finally it is possible to run the whole quantification procedure as a script as well. Using the script a batch of calculations can be performed.

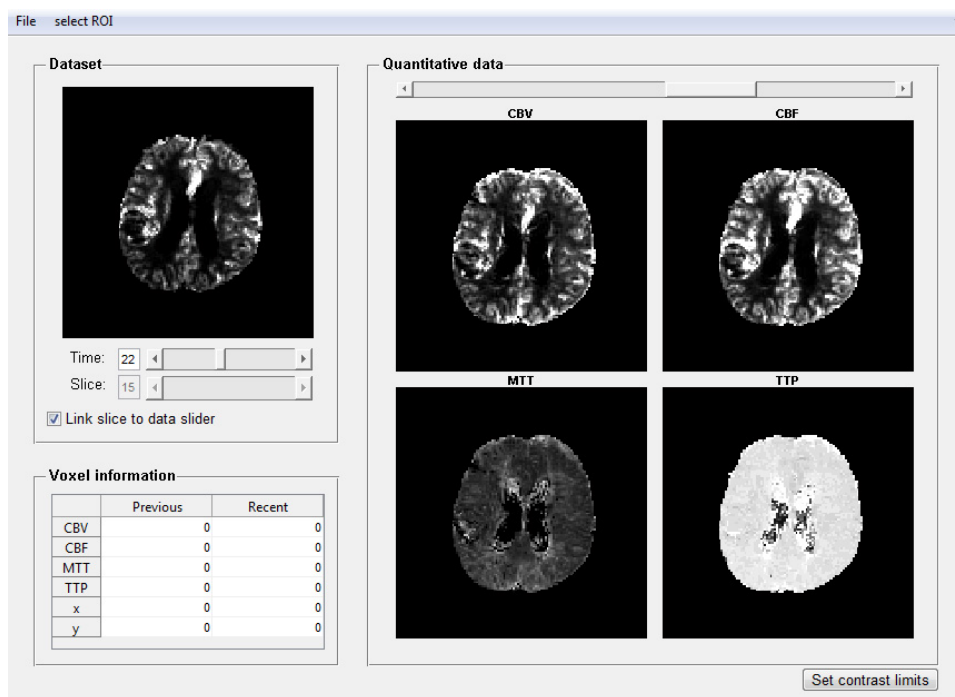


**Figure B.3:** A GUI to scroll through the final obtained CBV, CBF, MTT and TTP maps. Using the select ROI menu information about the selected region can be obtained.



---

## Bibliography

- [1] K.W. Muir, A. Buchan, R. von Kummer, J Rother, and J.C. Baron. Imaging of acute stroke. *Lancet Neurol*, 5(9):755–768, Sep 2006.
- [2] G. W. Albers. Expanding the window for thrombolytic therapy in acute stroke. The potential role of acute MRI for patient selection. *Stroke*, 30(10):2230–2237, Oct 1999.
- [3] O. Zaro-Weber, W. Moeller-Hartmann, W.D. Heiss, and J. Sobesky. The performance of MRI-based cerebral blood flow measurements in acute and subacute stroke compared with  $^{15}\text{O}$ -water positron emission tomography: identification of penumbral flow. *Stroke*, 40(7):2413–2421, Jul 2009.
- [4] M. Takasawa, P. Simon Jones, J. V. Guadagno, S. Christensen, T. D. Fryer, S. Harding, J. H. Gillard, G. B. Williams, F. I. Aigbirhio, E. A. Warburton, L. Østergaard, and J. Baron. How reliable is perfusion MR in acute stroke? Validation and determination of the penumbra threshold against quantitative PET. *Stroke*, 39(3):870–877, Mar 2008.
- [5] J.M. Warwick. Imaging of brain function using SPECT. *Metab Brain Dis*, 19(1-2):113–123, Jun 2004.
- [6] G. Rubin, A. D. Firlik, E. I. Levy, R. R. Pindzola, and H. Yonas. Xenon-enhanced computed tomography cerebral blood flow measurements in acute cerebral ischemia: Review of 56 cases. *J Stroke Cerebrovasc Dis*, 8(6):404–411, 1999.
- [7] J. Bews, K. St Lawrence, P. Dunscombe, B. McClarty, and M. Kroeker. A simplified method for measuring cerebral blood flow with Xenon-enhanced computed tomography. *Clin Phys Physiol Meas*, 12(3):279–287, Aug 1991.
- [8] T. E. Mayer, G. F. Hamann, J. Baranczyk, B. Rosengarten, E. Klotz, M. Wiesmann, U. Missler, G. Schulte-Altdorneburg, and H. J. Brueck-

- mann. Dynamic CT perfusion imaging of acute stroke. *AJNR Am J Neuroradiol*, 21(8):1441–1449, Sep 2000.
- [9] J. D. Eastwood, M. H. Lev, and J. M. Provenzale. Perfusion CT with iodinated contrast material. *AJR Am J Roentgenol*, 180(1):3–12, Jan 2003.
- [10] P. J. van Laar, J. van der Grond, W. P. T. M. Mali, and J. Hendrikse. Magnetic resonance evaluation of the cerebral circulation in obstructive arterial disease. *Cerebrovasc Dis*, 21(5-6):297–306, 2006.
- [11] D. Sanak, D. Horak, R. Herzig, P. Hlustik, and P. Kanovsky. The role of magnetic resonance imaging for acute ischemic stroke. *Biomed Pap Med Fac Univ Palacky Olomouc Czech Repub*, 153(3):181–187, Sep 2009.
- [12] T. T. Liu and G. G. Brown. Measurement of cerebral perfusion with arterial spin labeling: Part 1. Methods. *J Int Neuropsychol Soc*, 13(3):517–525, May 2007.
- [13] L. Østergaard. Principles of cerebral perfusion imaging by bolus tracking. *J Magn Reson Imaging*, 22(6):710–717, Dec 2005.
- [14] T. J. Carroll, V. Teneggi, M. Jobin, L. Squassante, V. Treyer, T. F. Hany, C. Burger, L. Wang, A. Bye, G. K. Von Schulthess, and A. Buck. Absolute quantification of cerebral blood flow with magnetic resonance, reproducibility of the method, and comparison with H<sub>2</sub>(15)O positron emission tomography. *J Cereb Blood Flow Metab*, 22(9):1149–1156, Sep 2002.
- [15] C. Westbrook and C. Roth. *MRI in practice*. Blackwell publishing, 3rd edition, 2005.
- [16] A. Villringer, B. R. Rosen, J. W. Belliveau, J. L. Ackerman, R. B. Lauffer, R. B. Buxton, Y. S. Chao, V. J. Wedeen, and T. J. Brady. Dynamic imaging with lanthanide chelates in normal brain: contrast due to magnetic susceptibility effects. *Magn Reson Med*, 6(2):164–174, Feb 1988.
- [17] K. L. Zierler. Theoretical Basis of Indicator-Dilution Methods For Measuring Flow and Volume. *Circ Res*, 10(3):393–407, March 1962.
- [18] J. Perkiö, H. J. Aronen, A. Kangasmki, Y. Liu, J. Karonen, A. Savolainen, and L. Østergaard. Evaluation of four postprocessing methods for determination of cerebral blood volume and mean transit time by dynamic susceptibility contrast imaging. *Magn Reson Med*, 47(5):973–981, May 2002.

- [19] O. Wu, L. L. Østergaard, R.M. Weisskoff, T. Benner, B.R. Rosen, and A.G. Sorensen. Tracer arrival timing-insensitive technique for estimating flow in MR perfusion-weighted imaging using singular value decomposition with a block-circulant deconvolution matrix. *Magn. Reson. Med.*, 50(1):164–174, 2003.
- [20] L. Knutsson, F. Sthlberg, and R. Wirestam. Aspects on the accuracy of cerebral perfusion parameters obtained by dynamic susceptibility contrast MRI: a simulation study. *Magn Reson Imaging*, 22(6):789–798, Jul 2004.
- [21] L. Knutsson, F. Sthlberg, and R. Wirestam. Absolute quantification of perfusion using dynamic susceptibility contrast MRI: pitfalls and possibilities. *MAGMA*, 23(1):1–21, Feb 2010.
- [22] L. Østergaard, R. M. Weisskoff, D. A. Chesler, C. Gyldensted, and B. R. Rosen. High resolution measurement of cerebral blood flow using intravascular tracer bolus passages. Part I: Mathematical approach and statistical analysis. *Magn Reson Med*, 36(5):715–725, Nov 1996.
- [23] F. Gul Aksoy and M. H. Lev. Dynamic contrast-enhanced brain perfusion imaging: Technique and clinical applications. *Seminars in Ultrasound, CT, and MRI*, 21(6):462 – 477, 2000. Advanced MR Imaging Techniques.
- [24] J. C. Kosior and R. Frayne. Perfusion parameters derived from bolus-tracking perfusion imaging are immune to tracer recirculation. *J Magn Reson Imaging*, 31(3):753–756, Mar 2010.
- [25] J. C. Kosior and R. Frayne. PerfTool: A software platform for investigating bolus-tracking perfusion imaging quantification strategies. *J. Magn. Reson. Imaging*, 25(3):653–659, 2007.
- [26] T. J. Carroll, H. A. Rowley, and V. M. Haughton. Automatic calculation of the arterial input function for cerebral perfusion imaging with MR imaging. *Radiology*, 227(2):593–600, May 2003.
- [27] K. A. Rempp, G. Brix, F. Wenz, C. R. Becker, F. Gckel, and W. J. Lorenz. Quantification of regional cerebral blood flow and volume with dynamic susceptibility contrast-enhanced MR imaging. *Radiology*, 193(3):637–641, Dec 1994.
- [28] K. B. Larson, W. H. Perman, J. S. Perlmutter, M. H. Gado, J. M. Ollinger, and K. Zierler. Tracer-kinetic analysis for measuring regional cerebral blood flow by dynamic nuclear magnetic resonance imaging. *J Theor Biol*, 170(1):1–14, Sep 1994.

- [29] L. Østergaard, D.A. Chesler, R.M. Weisskoff, A.G. Sorensen, and B.R. Rosen. Modeling cerebral blood flow and flow heterogeneity from magnetic resonance residue data. *J Cereb Blood Flow Metab*, 19(6):690–699, Jun 1999.
- [30] R. B. King, G. M. Raymond, and J. B. Bassingthwaite. Modeling blood flow heterogeneity. *Ann Biomed Eng*, 24(3):352–372, 1996.
- [31] J. J. Chen, M. R. Smith, and R. Frayne. Advantages of frequency-domain modeling in dynamic-susceptibility contrast magnetic resonance cerebral blood flow quantification. *Magn Reson Med*, 53(3):700–707, Mar 2005.
- [32] G. T. Gobbel and J. R. Fike. A deconvolution method for evaluating indicator-dilution curves. *Phys Med Biol*, 39(11):1833–1854, Nov 1994.
- [33] A. M. Smith, C. B. Grandin, T. Duprez, F. Mataigne, and G. Cosnard. Whole brain quantitative CBF and CBV measurements using MRI bolus tracking: comparison of methodologies. *Magn Reson Med*, 43(4):559–564, Apr 2000.
- [34] R. Wirestam, L. Andersson, L. Østergaard, M. Bolling, J. P. Aunola, A. Lindgren, B. Geijer, S. Holts, and F. Sthlberg. Assessment of regional cerebral blood flow by dynamic susceptibility contrast MRI using different deconvolution techniques. *Magn Reson Med*, 43(5):691–700, May 2000.
- [35] U. Sakoglu and R. Sood. Cerebral blood flow estimation from perfusion-weighted MRI using FT-based MMSE filtering method. *Magn Reson Imaging*, 26(3):313–322, Apr 2008.
- [36] W.H. Press, S.A. Teukolsky, W.T. Vetterling, and B.P. Flannery. *Numerical recipes in C*. Cambridge University Press, 2nd edn. edition, 1992.
- [37] S. Sourbron, R. Luybaert, P. Van Schuerbeek, M. Dujardin, and T. Stadnik. Choice of the regularization parameter for perfusion quantification with MRI. *Phys Med Biol*, 49(14):3307–3324, Jul 2004.
- [38] S. Sourbron, R. Luybaert, P. Van Schuerbeek, M. Dujardin, T. Stadnik, and M. Osteaux. Deconvolution of dynamic contrast-enhanced MRI data by linear inversion: choice of the regularization parameter. *Magn Reson Med*, 52(1):209–213, Jul 2004.
- [39] K. Murase, M. Shinohara, and Y. Yamazaki. Accuracy of deconvolution analysis based on singular value decomposition for quantification of cerebral blood flow using dynamic susceptibility contrast-enhanced

- magnetic resonance imaging. *Phys Med Biol*, 46(12):3147–3159, Dec 2001.
- [40] M. Smith, H. Lu, S. Trochet, and R. Frayne. Removing the effect of SVD algorithmic artifacts present in quantitative MR perfusion studies. *Magn. Reson. Med.*, 51(3):631–634, 2004.
- [41] F. Calamante, D. G. Gadian, and A. Connelly. Delay and dispersion effects in dynamic susceptibility contrast MRI: simulations using singular value decomposition. *Magn Reson Med*, 44(3):466–473, Sep 2000.
- [42] E. P. Vonken, F. J. Beekman, C. J. Bakker, and M. A. Viergever. Maximum likelihood estimation of cerebral blood flow in dynamic susceptibility contrast MRI. *Magn Reson Med*, 41(2):343–350, Feb 1999.
- [43] A. P. Dempster, N. M. Laird, and D. B. Rubin. Maximum Likelihood from Incomplete Data via the EM Algorithm. *Journal of the Royal Statistical Society. Series B (Methodological)*, 39(1):1–38, 1977.
- [44] L. Willats, A. Connelly, and F. Calamante. Improved deconvolution of perfusion MRI data in the presence of bolus delay and dispersion. *Magn Reson Med*, 56(1):146–156, Jul 2006.
- [45] I. K. Andersen, A. Szymkowiak, C. E. Rasmussen, L. G. Hanson, J. R. Marstrand, H. B W Larsson, and L. K. Hansen. Perfusion quantification using Gaussian process deconvolution. *Magn Reson Med*, 48(2):351–361, Aug 2002.
- [46] F. Zanderigo, A. Bertoldo, G. Pillonetto, and C. Cobelli. Nonlinear Stochastic Regularization to Characterize Tissue Residue Function in Bolus-Tracking MRI: Assessment and Comparison With SVD, Block-Circulant SVD, and Tikhonov. *IEEE transactions on biomedical engineering*, 56(5):1287–1297, May 2009.
- [47] E. J. Vonken, M. J. van Osch, C. J. Bakker, and M. A. Viergever. Measurement of cerebral perfusion with dual-echo multi-slice quantitative dynamic susceptibility contrast MRI. *J Magn Reson Imaging*, 10(2):109–117, Aug 1999.
- [48] F. Calamante, D. G. Gadian, and A. Connelly. Quantification of perfusion using bolus tracking magnetic resonance imaging in stroke: assumptions, limitations, and potential implications for clinical use. *Stroke*, 33(4):1146–1151, Apr 2002.
- [49] J. J. Chen, M. R. Smith, and R. Frayne. The impact of partial-volume effects in dynamic susceptibility contrast magnetic resonance perfusion imaging. *J Magn Reson Imaging*, 22(3):390–399, Sep 2005.

- 
- [50] L. Knutsson, D. van Westen, E. T. Petersen, K. Markenroth Bloch, S. Holts, F. Sthlberg, and R. Wirestam. Absolute quantification of cerebral blood flow: correlation between dynamic susceptibility contrast MRI and model-free arterial spin labeling. *Magn Reson Imaging*, 28(1):1–7, Jan 2010.
- [51] C. C. Quarles, D. F. Gochberg, J. C. Gore, and T. E. Yankeelov. A theoretical framework to model DSC-MRI data acquired in the presence of contrast agent extravasation. *Phys Med Biol*, 54(19):5749–5766, Oct 2009.
- [52] K. M. Johnson, J. Z. Tao, R. P. Kennan, and J. C. Gore. Intravascular susceptibility agent effects on tissue transverse relaxation rates in vivo. *Magn Reson Med*, 44(6):909–914, Dec 2000.
- [53] C. B. Grandin. Assessment of brain perfusion with MRI: methodology and application to acute stroke. *Neuroradiology*, 45(11):755–766, Nov 2003.
- [54] M. T. Madsen. A simplified formulation of the gamma variate function. *Phys. Med. Biol*, 37(7):1597–1600, 1992.
- [55] H. Gudbjartsson and S. Patz. The Rician distribution of noisy MRI data. *Magn Reson Med*, 34(6):910–914, Dec 1995.
- [56] F. Calamante, D. G. Gadian, and A. Connelly. Quantification of bolus-tracking MRI: Improved characterization of the tissue residue function using Tikhonov regularization. *Magn. Reson. Med.*, 50(6):1237–1247, 2003.
- [57] M. Salluzzi, R. Frayne, and M.R. Smith. An alternative viewpoint of the similarities and differences of SVD and FT deconvolution algorithms used for quantitative MKR perfusion studies. *Magn Reson Imaging*, 23:481–492, 2005.
- [58] L. Ko, M. Salluzzi, R. Frayne, and M. Smith. Reexamining the quantification of perfusion MRI data in the presence of bolus dispersion. *J Magn Reson Imaging*, 25(3):639–643, Mar 2007.
- [59] F. Calamante. Bolus dispersion issues related to the quantification of perfusion MRI Data. *Journal of magnetic resonance imaging*, 22:718–722, 2005.
- [60] B. Ebrahimi. *Cerebral blood flow measurement using MRI: Mathematical Regularization and Phantom evaluation*. PhD thesis, The university of michigan, 2008.

- 
- [61] B. Ebrahimi, S.D. Swanson, and T.E. Chupp. A Microfabricated Phantom for Quantitative MR Perfusion Measurements: Validation of Singular Value Decomposition Deconvolution Method. *IEEE transactions on Biomedical Engineering*,, 57:2730–2736, 2010.